THESIS

SYSTEMATIC RELATIONSHIPS BETWEEN OVERSHOOTING TOP CHARACTERISTICS AND ANVIL LIFE CYCLE OBSERVED WITH GEOSTATIONARY SATELLITES

Submitted by

Rachael M. Auth

Department of Atmospheric Science

In partial fulfillment of the requirements

For the Degree of Master of Science

Colorado State University

Fort Collins, Colorado

Spring 2026

Master's Committee:

Advisor: Susan C. van den Heever

Sean Freeman
Kristen Rasmussen
Steven Reising

ABSTRACT

SYSTEMATIC RELATIONSHIPS BETWEEN OVERSHOOTING TOP CHARACTERISTICS AND ANVIL LIFE CYCLE OBSERVED WITH GEOSTATIONARY SATELLITES

Deep convective storms with strong updrafts generate robust anvils and distinct cloud top structures. These structures, including overshooting tops (OTs) and above-anvil cirrus plumes (AACP), can be routinely identified atop the most powerful storms on the planet and are often indicative of severe weather, including tornadoes and large hail. The overarching goal of this study is to assess how OT characteristics are related to the structural and temporal properties of their parent anvils.

Derived anvil cloud statistics from a robust database of tracked anvils and OTs using rapid scan geostationary satellite data are presented. A novel approach to identifying and tracking storm systems through their life cycle, using *tobac*'s family tracking capabilities, was leveraged to create the database over four U.S. convective seasons. Just over 25% of nearly 61,000 identified anvils were associated with at least one OT. Analysis reveals that the mean OT lifetime was ~8.5 minutes, less than the current cadence of global full-disk geostationary satellite observations (10 minutes). OT count was found to be greatest during the mature stage of the anvil life cycle, and anvils also often overshoot for more than 20 minutes.

The results shown here suggest that the most important predictors of anvil size and lifetime are OT height and count, rather than OT area or lifetime as previously hypothesized. The results also show that taller OTs are spatially larger than shallower OTs, suggesting that larger updrafts can transport more mass higher in the atmosphere. This study therefore reveals key

relationships between OTs and their parent anvils and motivates future observations of updrafts and convective mass flux (CMF) from upcoming missions such as INCUS.

ACKNOWLEDGEMENTS

This document would not have been possible without support from an amazing team of people invested in its success. First, I would like to thank my advisor, Dr. Sue van den Heever for her mentorship and encouragement. Being the first student on INCUS has been an incredible experience and I couldn't be more grateful to be a part of the team. Thank you also to Kristen Rasmussen, Steve Reising, and Sean Freeman for serving on my committee and giving thoughtful feedback during the writing process. The co-authors on this paper, Kris Bedka, John Cooney, and Sean Freeman sacrificed so much time and energy into tailoring their algorithms for the goals of the research and it truly would not have been possible without their time and dedication. I would also like to thank my undergraduate advisor, Cameron Homeyer, for giving me my first research opportunity, including the chance to participate in a field campaign, learn about the publication process by writing a first author paper, and becoming fascinated with all phenomena around the tropopause in general. We own the sky! During my time at CSU, I've also received incredible emotional and technical support from friends and staff at the department. Thank you to all van den Heever group members past and present, including Steve Saleeby, Dr. Leah Grant, Dr. Peter Marinescu, Dr. Brenda Dolan, Dr. Rick Schulte, Dr. Randy Chase, Dr. IT Singh, Dr. Jennie Bukowski, Dr. Sean Freeman, Dr. Nick Falk, Dr. Bee Leung, Christine Neumaier, Ben Ascher, Charles Davis, Phoebe Lin, Andrew Muehr, and Miles Hamala. Lastly, I would like to acknowledge that this work was supported by INCUS, a NASA Earth Venture Mission, funded by NASA's Science Mission Directorate and managed through the Earth System Science Pathfinder Program Office under contract number 80LARC22DA011.

TABLE OF CONTENTS

Chapter 1 INTRODUCTION

1.1 Background and motivation

Deep convection with strong updrafts that overshoot their level of neutral buoyancy (LNB) can cross the tropopause and inject cloud matter into the stratosphere. This process generates distinct cloud top features such as overshooting tops (OTs) and above-anvil cirrus plumes (AACPs). These features are visible in satellite imagery as bubbling, textured areas and 'v-signatures' embedded within the storm's anvil shield (K. Bedka et al., 2010; Setvák et al., 2013), and they contribute to the irreversible, bidirectional mixing of trace gases across the tropopause (Anderson et al., 2012). This stratospheric-troposphere exchange (STE) can perturb the atmospheric thermal structure near the tropopause and generate gravity waves that propagate into the lower stratosphere (Gordon & Homeyer, 2022). OTs and AACPs are also associated with severe weather on the ground including hail, strong winds, and tornadoes (Bedka et al., 2018; Dworak et al., 2012; Homeyer et al., 2017). Despite extensive study of OTs and their associated storms, the statistical relationships between OT behavior and their parent anvils, including anvil evolution, remain poorly quantified, thus limiting our ability to connect OTs to storm intensity diagnostics and upper-tropospheric–lower-stratospheric (UTLS) transport processes. As such, characterizing OTs and their relationships to their parent anvils throughout the storm life cycle forms the focus of this thesis.

Tropopause-overshooting convection is responsible for the rapid transport of trace gases into the UTLS, sometimes irreversibly altering the concentration and distribution of greenhouse gases such as water vapor and ozone within these regions (Anderson et al., 2012). An indirect transport pathway common in the tropics involves overshooting convection detrainment in the

tropical upper troposphere, followed by ascent into the stratosphere via the Brewer-Dobson circulation (Holton et al., 1995) While this mechanism is thought to be the primary source of stratospheric hydration in the tropics, it is also relatively slow because convective updrafts are less likely to overshoot in regions with a higher, colder tropical tropopause characteristic of the tropics. In the midlatitudes, direct hydration via detrainment of water vapor and sublimation of lofted ice can bypass this bottleneck and penetrate several kilometers into the lower stratosphere (LS) (Jensen et al., 2020).

Convection-resolving model simulations have estimated that overshooting convection contributes between 10 and 15% of the global LS water vapor budget (Dauhut & Hohenegger, 2022; Dessler & Sherwood, 2004; Tinney & Homeyer, 2021; Ueyama et al., 2023). Past studies using both in situ and remote sensing observations have attempted to validate these estimates. These include a 10-year analysis of NEXt generation RADar (NEXRAD) observations conducted by Cooney et al. (2018) and in situ observations made on the ER-2 during the Dynamics and Chemistry of the Summer Stratosphere (DCOTSS) mission, both of which demonstrate that the stratosphere is routinely hydrated by convection (Gordon et al., 2024; Homeyer et al., 2023).

A far less observed pathway for STE is the transport of stratospheric air in the downward direction, or stratosphere-to-troposphere transport (STT). Limited in situ observations and modeling studies have focused on one known mechanism termed anvil wrapping, in which ozone-rich stratospheric air is transported downward around the anvil edge and into the upper troposphere (Auth & Homeyer, 2023; Pan et al., 2014; Phoenix et al., 2020; Poulida et al., 1996). Apart from this mechanism, however, the dynamics and quantification of STT in tropopause-overshooting convection remain poorly constrained in the literature. Because many of the

dynamical processes governing both upward and downward exchange are tied to the evolution and persistence of overshooting updrafts, improved characterization of OT life cycle behavior may provide indirect constraints on both STE and STT processes.

Modeling studies aimed at understanding the dynamics of STE and STT mass exchange processes have revealed that AACP formation is driven by the development of a hydraulic jump around an OT acting as a topographic barrier (Bedka et al., 2018; O'Neill et al., 2021). The subsequent breaking of gravity waves downstream of the oscillating OT can promote the transport of water vapor into the lower stratosphere (Gordon et al., 2024; Homeyer et al., 2017). Other turbulent mixing processes, such as Kelvin-Helmholtz instabilities and tropopause-level shallow circulations associated with differential advection have also been shown in model simulations to contribute to irreversible mixing at cloud top (Gordon & Homeyer, 2022; Pan et al., 2014; Phoenix et al., 2020).

The amount of convective mass flux (CMF) associated with STE is sensitive to storm morphology and environment. For example, Bigelbach et al. (2014) found that supercells are associated with larger updrafts and deeper overshoots compared to other storm modes, whereas mesoscale convective systems (MCSs) are associated with more STE by having a greater number of weaker overshoots. Variations in LS static stability can also modulate properties of deep convection. Environments with weaker static stability were found to enable deeper overshooting and thus more STE (Berman et al., 2024; Homeyer et al., 2014).

Previous research has established a fundamental relationship between vertical velocity and anvil formation (Ritman et al., 2026; Senf et al., 2015). There is also strong observational and modeling evidence for the relationship between OT metrics and updraft intensity, but there has been less focus on finding the connection between OT intensity and anvil properties (Berman et

al., 2025; Christo et al., 2025; Fujita, 1974; Jellis et al., 2023; Marion et al., 2019; Trapp et al., 2017). Because previous literature has demonstrated that OT behavior is linked to storm-scale updraft intensity, and that updraft intensity drives the CMF required to grow anvils, understanding the evolution of OT and anvil properties, as well as OT–anvil relationships would provide a unified framework for studying convective transport, atmospheric dynamics, and STE. This thesis intends to take this a step further by additionally quantifying the systematic connections between OTs and their parent anvils which is critical for understanding the broader dynamical and compositional impacts of overshooting convection.

1.2 Thesis outline and objectives

The overarching objective of this thesis is to investigate how anvil clouds are related to the spatial and temporal evolution of overshooting updrafts. More specifically, we seek to expand our current understanding of the relationships between the characteristics of OTs and their parent anvils by asking the following questions:

1. How many distinct OTs is an individual anvil associated with, and at what point in the anvil life cycle does OT count peak?
2. How do OT structural characteristics (height, area, and lifetime) vary with one another?
3. How does brightness temperature fluctuate throughout OT lifetime?
4. Are storms with more OTs associated with longer lived and/or larger anvils than storms with fewer OTs?
5. How do OT structural characteristics scale with anvil size and anvil lifetime?

To achieve these goals, we build separate OT and anvil databases from the Geostationary Operational Environmental Satellite (GOES-R) East rapid scan M1 sector visible and infrared imagery for four convective seasons (March-August) from 2022-2025. First, areas of overshooting convection identified by a deep learning objective OT detection model are tracked with an object-based cloud tracking algorithm (Cooney et al., 2025). Similarly, anvil clouds are identified and tracked with the same algorithm, and a novel 'family tracking' approach (Freeman et al., 2024; Heikenfeld et al., 2019; Sokolowsky et al., 2024) is used to assign each anvil a unique ID and link OTs to the anvils in which they are located. From this, storm-level information about area, brightness temperature, lifetime, OT count, and cloud top height are available for all anvil and OT objects.

We hypothesize that the growth and decay of storm anvil clouds are intrinsically linked to OT properties, such that OT number, peak timing, and structural characteristics, show measurable relationships with anvil size and lifetime and with one another. The introduction, methods, and results from this study, titled "Systematic Relationships Between Overshooting Top Characteristics and Anvil Life Cycle Observed with Geostationary Satellites," are presented in Chapter 2 of this thesis and have been prepared for submission to the *Journal of Geophysical Research*. The overall summary and conclusions from the research presented in this thesis are provided in Chapter 3.

Chapter 2 SYSTEMATIC RELATIONSHIPS BETWEEN OVERSHOOTING TOP CHARACTERISTICS AND ANVIL LIFE CYCLE OBSERVED WITH GEOSTATIONARY SATELLITES [1]

2.1 Introduction

Thunderstorms with strong updrafts are capable of overshooting their LNB, penetrating the tropopause, and entering the lower stratosphere. Such deep convective storms can influence STE, perturb the atmospheric thermal structure near the tropopause, and generate gravity waves that propagate into the lower stratosphere. They are also often associated with severe weather hazards including strong winds, large hail, and tornadoes (Bedka et al., 2018; Dworak et al., 2012; Homeyer et al., 2017). Thunderstorms frequently produce features with pronounced signatures in visible (VIS, e.g. 0.64 μm) and infrared (IR, e.g. 10.3 μm) satellite imagery, such as OTs and AACPs (Bedka et al., 2010, 2018; Setvák et al., 2013b). OTs typically appear as localized regions of textured, elevated cloud tops in VIS imagery, and as colder infrared brightness temperatures (BTs) relative to the warmer surrounding anvil cloud (Bedka & Khlopenkov, 2016). As OTs are indicative of strong updraft intensity and tropopause penetration, characterizing not only OT-anvil relationships, but also their evolution with respect to anvil life cycle, provides insight into severe weather processes and UTLS dynamics. A systematic investigation of OT behavior over the United States, particularly with respect to their parent anvil clouds, is therefore critical for understanding their broader dynamical and compositional impacts.

[1] This study, titled "Systematic Relationships Between Overshooting Top Characteristics and Anvil Life Cycle Observed with Geostationary Satellites" (Auth, R., Bedka, K., Cooney, J., Freeman, S., and van den Heever, C., 2026), has been prepared for submission to the *Journal of Geophysical Research*.

Studies using both in situ and remote sensing observations have investigated the impact of deep convection on UTLS composition. Overshooting convection is estimated by convection-resolving model simulations to contribute roughly 10-15% of the global LS water vapor budget (Dauhut & Hohenegger, 2022; Dessler & Sherwood, 2004; Tinney & Homeyer, 2021; Ueyama et al., 2023). There have been observational attempts to validate these estimates, including a 10-year analysis of NEXRAD radar observations conducted by Cooney et al. (2018), which suggests that approximately 50% of tropopause-overshooting events impact the stratosphere. Complementary in situ observations made on the ER-2 during the DCOTSS mission demonstrate that the stratospheric overworld is frequently hydrated by convection, sometimes exceeding background water vapor concentrations by more than a factor of two at altitudes up to 2.3 km above the tropopause (Gordon et al., 2024; Homeyer et al., 2023).

The amount of CMF associated with UTLS transport pathways is sensitive to storm characteristics, such as storm morphology, and is also modulated by the environments they populate. For example, Bigelbach et al. (2014) found that isolated supercells exhibit larger updrafts and deeper overshoots compared to other storm modes, while MCSs have a greater number of weaker overshoots that were able to achieve more overall STE. Additionally, variations in LS static stability can constrain properties of deep convection, with weaker static stability enabling deeper overshooting (Berman et al., 2024; Homeyer et al., 2014).

Previous research has found a strong, positive correlation between metrics of OT area, updraft intensity, hail size, and tornado intensity, but there is less supporting evidence for a relationship between OT area and anvil area (Berman et al., 2025; Christo et al., 2025; Fujita, 1974; Jellis et al., 2023; Marion et al., 2019; Trapp et al., 2017). Cloud top detrainment measurements presented by Apke et al. (2018) also suggest that OTs classified as severe

(associated with a thunderstorm that produces a tornado, winds of at least 58 mph, and/or hail at least 1" in diameter) have stronger inferred updrafts than OTs associated with non-severe deep convection. In addition, severe storms tend to exhibit more prominent and persistent OTs than non-severe storms. These findings suggest that the structural characteristics of OTs hold physically meaningful information about storm intensity, environmental static stability, and cross-tropopause transport efficiency. At the same time, it is well established that updraft strength (and thus CMF) drives anvil initiation and growth (Ritman et al., 2026; Senf et al., 2015). If this is the case, systematic relationships should exist between OT structural properties (including height, area, and lifetime) and the temporal and geometric evolution of their parent anvils.

Despite its well-studied impacts on the environment and at the surface, overshooting convection remains underrepresented in numerical weather prediction (NWP) systems. Echo top heights predicted by the High-Resolution Rapid Refresh (HRRR) were generally about 2 km lower than those of ~75,000 individual updrafts observed using ground-based radar in the United States. Furthermore, only 4% of the HRRR overshoots reached the stratospheric overworld, compared to 35% of the observed overshoots reaching that level (Bissell et al., 2024). These results reveal a large, systematic underestimation of predicted OT depth and detrainment levels by our current weather forecasting models, with implications for the associated weather hazards discussed above. In addition to shortfalls in severe weather prediction, global climate models (GCMs) do not resolve deep convective transport processes, including the stratospheric moistening and cooling induced by overshooting convection (Solomon et al., 2010). Thus, errors in the estimates of the chemical and radiative impacts of overshooting convection and cross-

tropopause exchange permeate modeling systems across scales, from NWP to GCMs (Berman et al., 2024; Pan et al., 2014).

Overshooting convection has been studied at the global scale using the National Aeronautics and Space Administration's (NASA) Global Precipitation Mission (GPM) and the Tropical Rainfall Measurement Mission (TRMM) precipitation feature data sets (C. Liu & Zipser, 2005; N. Liu et al., 2020), the Aura Microwave Limb Sounder (MLS) (Tinney & Homeyer, 2021), as well as with CloudSat, Cloud-Aerosol Lidar and Infrared Pathfinder Satellite Observations (CALIPSO), and Moderate Resolution Imaging Spectroradiometer (MODIS) (Bedka et al., 2010, 2015; Takahashi & Luo, 2014). Newer missions such as NASA's Earth Cloud, Aerosol and Radiation Explorer (EarthCARE) (Illingworth et al., 2015) and the upcoming INvestigation of Convective UpdraftS (INCUS) mission (Dolan et al., 2023; Prasanth et al., 2023; van den Heever, 2021) will produce novel 3D observations of deep convection, thereby advancing our understanding of OT dynamics. While the storm observations made by these satellites may provide information on OT frequency and depth, some of their orbital pathways limit their ability to resolve the rapid evolution of cloud-top features and to capture their full diurnal variability. Furthermore, given the relatively small horizontal extent of OTs, they are typically infrequently sampled in these databases due to the narrow swaths of the instruments involved (e.g. only 111 OTs were observed by CloudSat from April 2008 to September 2009 (Bedka et al., 2012)). Conversely, the Geostationary Operational Environmental Satellite (GOES-R) rapid scan Mesoscale Domain Sector (MDS) imagery provides updates every 30 seconds to one minute. Such high-temporal resolution observations from geostationary satellites are therefore better suited for detecting and evaluating OT life cycle and diurnal variation, although they cannot capture the vertical structure of OTs.

Hand analysis of these rapidly evolving OT features within the extensive GOES-R MDS datasets is extremely time consuming and often difficult to achieve with the human eye alone. As such, automated detection OTs and AACPs has advanced greatly in recent years thereby facilitating the identification of such features, as has the emergence of machine learning (ML) approaches (Berendes et al., 2008; Cintineo et al., 2020; Kim et al., 2018). ML approaches provide many benefits over simpler approaches to satellite-based object detection of OTs. Traditional methods have relied on single-pixel processing based on IR temperature thresholds and / or multispectral analysis, such as calculating brightness temperature differences between the 6–7 μm water vapor absorption band and 12 μm channels (Bedka et al., 2010; Khlopenkov et al., 2021; Mikuš & Strelec Mahović, 2013; Setvák et al., 2013a). Although many regional OT databases have been successfully developed from these methods (e.g. Bedka et al. 2010; Bedka 2011; Bedka et al. 2018; Punge et al. 2017; Proud 2015; Thiery et al. 2016), feedback from operational users and researchers have indicated that a simple yes / no binary detection mask was undesirable because it often missed true OTs (Khlopenkov et al., 2021). This led to the development of probabilistic output that characterizes specific OT properties, rather than relying on fixed detection criteria. Furthermore, deep learning models allow for user-friendly and broadly applicable products that can approximate the human identification process in real time (Cooney et al., 2025). Most recently, a novel, open-source OT and AACP detection method has been developed that is further facilitating OT research (Cooney et al., 2025).

In conjunction with automated detection methods, object-based tracking frameworks like the Tracking and Object-Based Analysis of Clouds (*tobac*) and the Storm Labeling in 3 Dimensions (SL3D) allow for the analysis of full storm life cycles using two- and three-dimensional data fields (Freeman et al., 2024; Heikenfeld et al., 2019; Sandmæl et al., 2019;

Sokolowsky et al., 2024). To date, only a handful of studies have used *tobac* for OT tracking (Itterly et al., 2025; Scarino et al., 2023), and none have leveraged *tobac*'s newly developed family tracking capability to track overshooting convection throughout its entire life cycle. This *tobac* capability enables a systematic examination of how OT structure evolves relative to the life cycle of its parent anvil.

These advancements in the full life cycle tracking of anvils and embedded OTs now make it feasible to test whether OT properties are systematically related to anvil life cycle, and vice- versa. We hypothesize that the life cycle of storm anvil clouds is intrinsically linked to OT properties, such that OT count, area, height, and lifetime show measurable relationships with anvil size and lifetime and with one another. Failure to identify such relationships would indicate that anvil evolution is only weakly related to OT properties, and thus to storm updraft speed and geometry.

To test these hypotheses, we investigate how OT characteristics are related to the structural and temporal properties of their parent anvils. More specifically, we ask the following questions:

1. How many distinct OTs is an individual anvil associated with, and at what point in the anvil life cycle does OT count peak?
2. How do OT structural characteristics (height, area, and lifetime) vary with one another?
3. How does brightness temperature fluctuate throughout OT lifetime?
4. Are storms with more OTs associated with longer lived and/or larger anvils than storms with fewer OTs?
5. How do OT structural characteristics scale with anvil size and anvil lifetime?

We address these questions using geostationary satellite observations, ML-based OT detections, and the *tobac* object-based tracking algorithm.

2.2 Data and Methods

a Deep Learning Objective OT Detection Software (MLv3.2)

OT detections were obtained using v3.2 of NASA's Deep Learning Objective OT Detection Software (Cooney et al., 2025) applied to the National Oceanic and Atmospheric Administration (NOAA)/NASA GOES-16 and GOES-19 Advanced Baseline Imager (ABI) data for the four most recent Northern Hemisphere convective seasons (March-August) of 2022, 2023, 2024, and 2025. The ABI instrument has multiple scan modes available with different temporal and spatial resolutions. Based on the typical scale of OTs (~12 km average diameter and <10 min average lifetime; Fujita 1974; Liu and Zipser 2005; Bedka et al. 2010), the Mesoscale Domain Sector (MDS) mode was selected for this study, which provides images every 1-min. Importantly, the MDS is used for real time monitoring of severe weather conditions and these operations can be requested by local and federal entities over any area of the full disk domain. A heatmap of the mesosector locations for this study period is shown in Figure 1a. It is clear from this figure that the majority of GOES-East MDS observations are concentrated over the default viewing area (New England). Other frequently observed areas cover most of the central/south central U.S, including Kansas, Oklahoma, Texas, Arkansas, and Missouri. OT detections made during the day used the vis_tropdiff model (Cooney et al., 2025), which ingests VIS and IR imagery, while at night, the IR-only tropdiff model (Cooney et al., 2025), was selected. Both models regrid the IR data to the VIS grid, which has a spatial resolution of 0.5 km and a temporal frequency of 1 min. More details as to how the input data are prepared can be found in (Cooney et al.(, 2025). The output of the ML algorithm for each timestep consists of the

regridded GOES data (VIS radiances or IR brightness temperatures), 6-hourly GFS tropopause temperatures interpolated to the GOES grid, and the OT probabilities (0-1) at each pixel. The next paragraph details the OT probabilities.

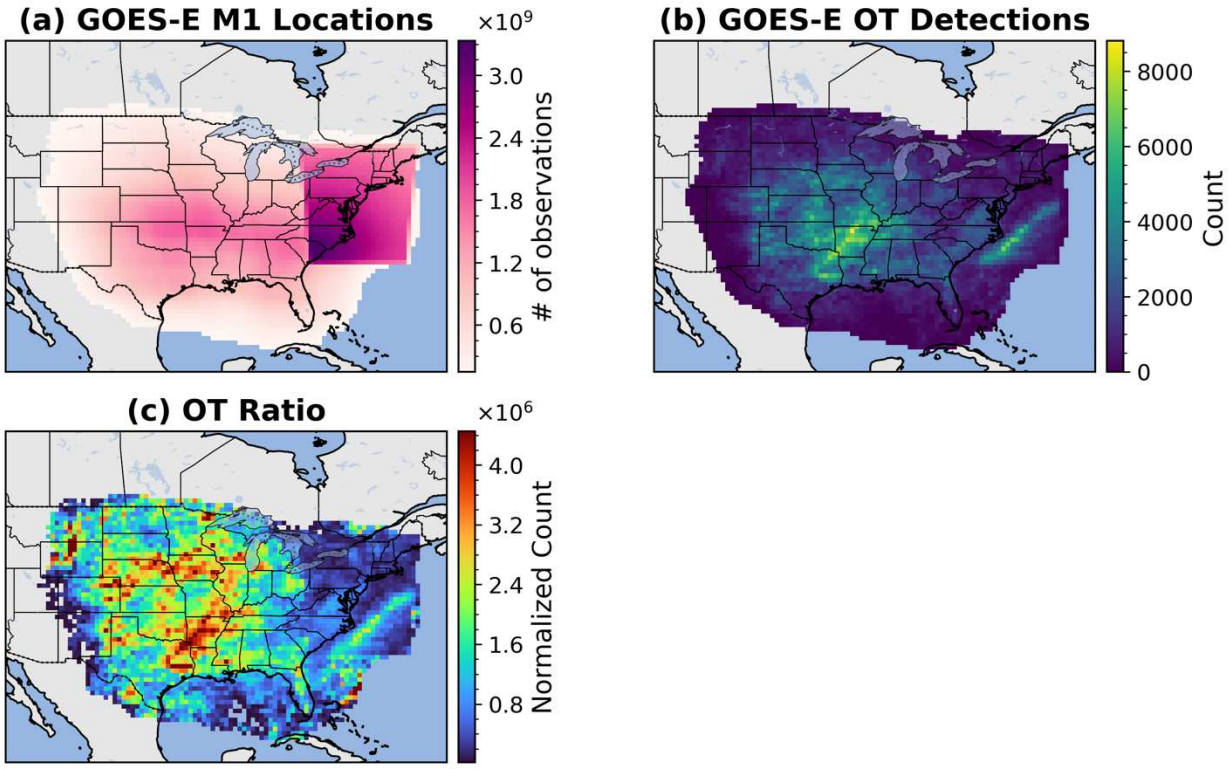

Figure 1. Spatial distribution maps created from the OT database during March-August 2022-2025 show that OTs are most frequent through the south and central great plains. (a) GOES-E Meso 1 (M1) locations colored by the density of observations. (b) Identified OT locations colored by the density of observations. (c) Ratio of the number of OTs to the number of GOES-E M1 observations at each grid point, colored by normalized OT fraction.

Each model has its own optimal OT probability threshold determined by the peak of its critical success index (CSI) (Cooney et al., 2025). The optimal thresholds for vis_tropdiff and tropdiff models were originally set to 0.1 and 0.65, respectively. However, since the release of v3.2 of the tropdiff model, input and further assessments by the software's developers (Bedka and Cooney, pers. comm) revealed that the 0.65 threshold appears to be too conservative,

reducing the false alarm rate at the expense of missing 'true' detections. While this may be an optimal choice for real-time forecasting of severe weather, achieving the goals of the research described here relies on confident, consistent detections through time. Extensive testing and validation of the model with NEXRAD observations demonstrated that the original optimal threshold values of 0.1 for the daytime model and a less conservative threshold of 0.4 for the nighttime model (which yielded > 75% Probability of Detection (POD) with ~30% False Alarm Rate (FAR) when validated against human-labeled OTs for three independent test cases) were the most appropriate thresholds for achieving these goals.

b Tracking and Object-based Analysis of Clouds (tobac)

To document overshooting storms throughout their entire life cycle, we first built a database of anvil cloud objects and then populated them with their corresponding identified and tracked overshoots. A schematic of the entire workflow, including the *tobac* pipeline, is provided in Figure 2. The anvil object centroids were identified as "features", tracked in time, and then segmented using *tobac* version 1.6.2 (Community et al., 2025; Heikenfeld et al., 2019; Sokolowsky, Freeman et al., 2024) to produce area masks for each feature. A list of all the applied *tobac* threshold values and their descriptions are provided in Table 1. The selected anvil threshold values were based on those tested and applied in Itterly et al. (2025) (adjusted for the high spatial-temporal resolution of the data used in this study). The exception to this was the switch from the single threshold (-20K anvil-tropopause brightness temperature difference (BTD)) used in Itterly et al. (2025) to a multi-threshold approach (-20K, -10K, and 0K anvil-tropopause BTD). For the purposes of this project, multi-thresholding allowed for more accurate identification of individual anvil features across a range of cloud-top brightness temperatures and

hence facilitated identifying anvils earlier in their life cycle when their cloud top temperatures are warmer. Anvil IR brightness temperatures and tropopause temperatures (see section 2.2.a) were extracted from the netCDF files generated by the ML OT detection model (Cooney et al., 2025). During segmentation, statistics such as area and minimum brightness temperature were calculated for each anvil feature. These are discussed more in depth in section 2.2.c.

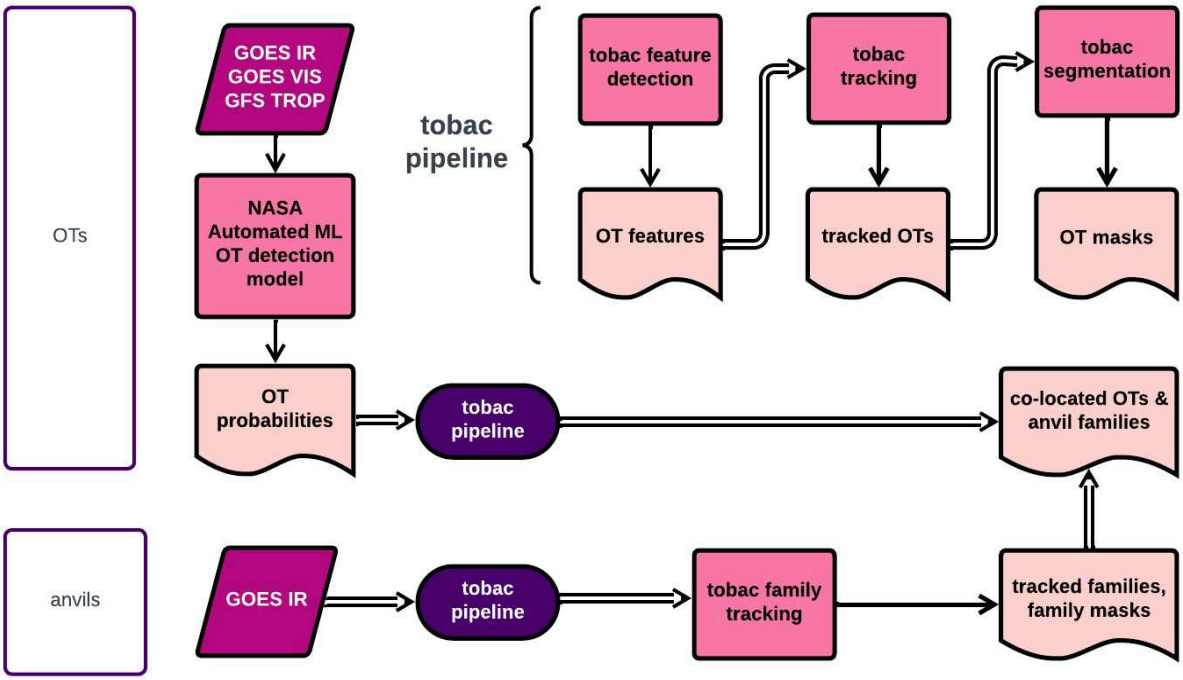

Figure 2. A flowchart illustrating how the OT and anvil databases are created and joined together. As described in the text, GOES IR data and GFS tropopause data are fed into the *tobac* pipeline, and then anvils are tracked in time as "families". OT probabilities from the ML model are fed into the *tobac* pipeline and then co-located with the tracked anvils.

A downside to using the standard segmentation function in *tobac* for this goal is that single anvils can be broken into multiple features, which does not allow for complete storm-relative lifetime analysis. To overcome this challenge, we utilized a newly developed feature of *tobac* referred to as 'families'. This function allows for a unique family ID number to be

assigned to all segmentation areas that are touching (Freeman et al., 2024). These families were then tracked through time, such that each individual anvil area retained a unique family ID through its entire lifetime (except for the case of mergers/splits, which is discussed below). These IDs were then later used to connect each OT to its corresponding parent storm.

The workflow for identifying families and then tracking them through time starts similarly to segmentation. The input data are thresholded again, this time at only a single value (-20K anvil-tropopause BTD in this case). All already identified features within this threshold boundary are grouped into a single convective "family." Each family has at least one identified feature, and there is no limit to the maximum number of features per family. The approach of collecting individual features into a single family allows for multiple, small-scale convective features to be grouped into a single overarching anvil cloud (see the example below).

The identified families are then tracked using the information from each family's constituent features. For simple cases (e.g., one tracked family with three constituent tracked features at t_0, and the same three constituent tracked features in a family at t_1), the family at t_0 and t_1 are immediately linked, and the resulting tracked family is assigned the same ID number at all the times that it is present. This remains true if one of the tracked features is no longer identified as a discrete feature at t_1, or a new tracked feature appears as a constituent feature in the family identified at t_1. For more complex cases involving storm mergers and storm splits, and hence a family merger or split, where there is not a one-to-one mapping between tracked features and families between t_0 and t_1, a more complex processing workflow is required. For splits, the family number is continued if there is a resulting family at t_1 where the ratio of the area of the splitting, parent family (at t_0) and the family of one of the children (at t_1) and the inverse ratio are both greater than 30%, resulting in the child family being of similar size to the parent family.

This prevents children that are much smaller than the parent family from being identified as the same family over time, preventing sudden jumps in identified family area. For mergers, the family number of the resulting merged family at t_1 is selected as the largest of the combining parent t_0 families, subject to the same 30% area-ratio criterion applied to splits, again requiring them to be of similar size. The 30% area-ratio criterion was selected following sensitivity testing and ensures continuity of dominant anvil structures while preventing spurious linking of more marginal features.

Figure 3 shows an example of how anvils are identified and tracked within the "family" framework described above. At the first timestep (panel a), convection initiates and the temperature of the cloud is warmer than the anvil BTD thresholds required, so no anvil (family) is identified. At the second timestep (panel b), the anvil BTD thresholds are met, and the identified anvil is labeled with a family ID #1. By the third timestep (panel c), two more anvils meet the anvil threshold are identified and labeled as family ID #2 (upper), and family ID #3 (lower). In the last timestep shown (panel d), the anvil labeled as family ID #3 has merged with family ID #1. According to the size requirements for relabeling laid out in the section above, the smaller anvil (family ID #3) is relabeled as family ID #1. This ensures that the OTs with the anvil labeled family ID #1 are associated with a consistent family ID that can be used for full storm life cycle analysis. For the OT that was originally associated with family ID #3, this merger into family ID #1 would also be recorded.

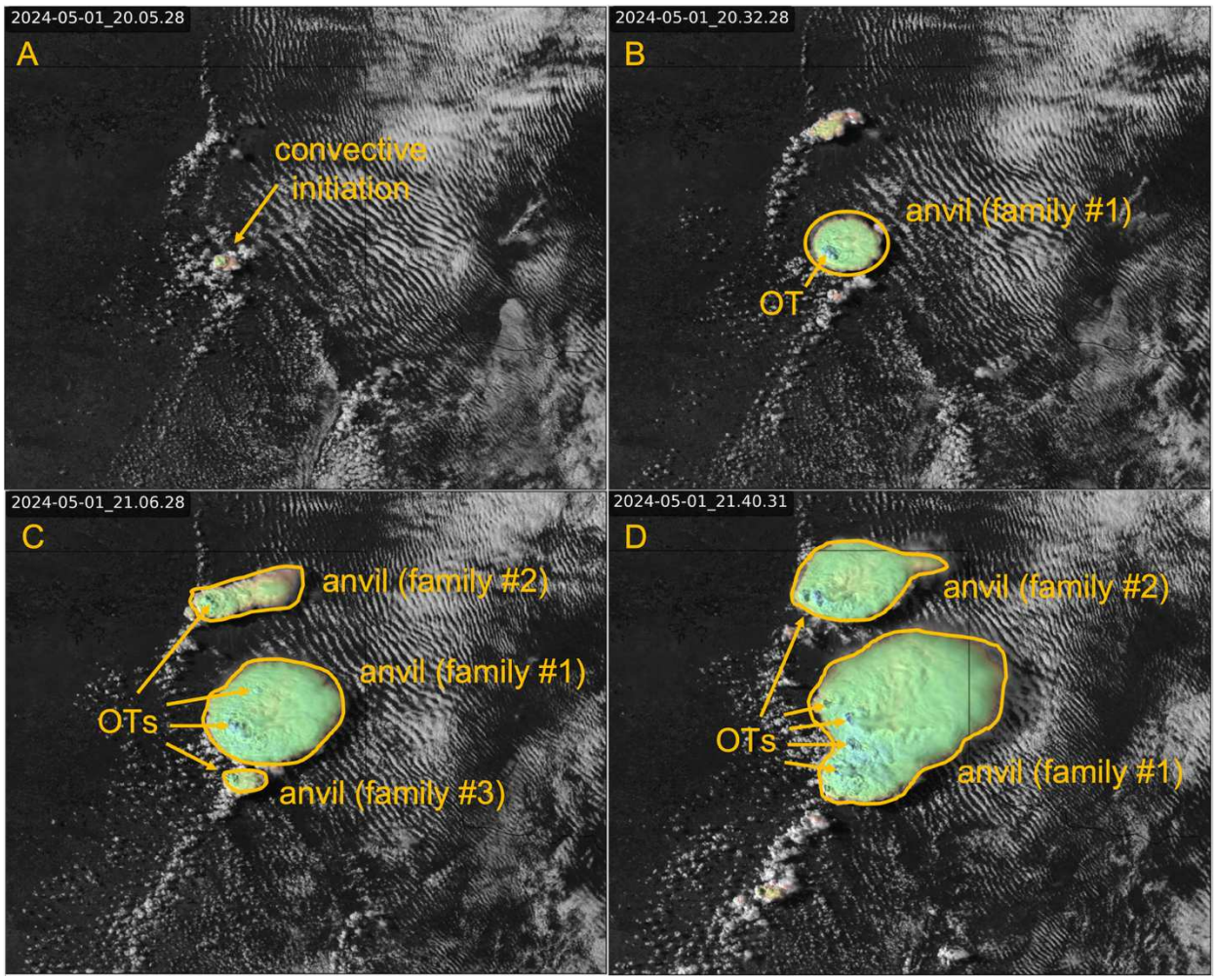

Figure 3. GOES-E visible satellite imagery at four different times depicting the evolution of cloud top features and how anvils are organized into "families" when using *tobac* to conduct anvil tracking. Arrows point to OTs, while anvils and families are circled and labelled appropriated (see the text for more details).

OTs were identified as "features" and tracked as "cells" based on the vis_tropdiff and tropdiff model outputs (Cooney et al., 2025) using the thresholds shown in Table 1. In addition to the detection thresholds defined in section 2.2.a, other *tobac* identification and tracking parameters were set based on known physical values attributed to OTs and their environments. For example, min_distance was set to 10 km by taking the average of typical OT diameters found in the literature, which ranges from 1-20 km, and assuming that if the typical OT is 10km wide, then there shouldn't be another OT within 10km (Bedka et al., 2010; Brunner et al., 2007;

Fujita, 1974; N. Liu et al., 2020). Similarly, the threshold used for time_cell_min (2 min) was constrained by the typical lifetime of OTs (< 10 minutes, (Setvák et al. 2013; Bedka et al. 2015), as well as the temporal resolution of the dataset (1 min). The value 125 ms^{-1} was chosen for vmax to represent the maximum expected value of stratospheric winds (Manney et al., 2017). Sensitivity testing indicated that the primary OT statistics and scaling relationships were not sensitive to small perturbations in the selected threshold values. OT tracking, segmentation, and statistics calculations (centroid minimum brightness temperature and tropopause-relative OT height) were performed with the same *tobac* pipeline used to build the anvil database and are described in section 2.2.c.

Table 1. Feature detection, segmentation, and linking settings used in *tobac* for anvil and OT object detection and tracking.

Parameter	Description	Anvils	OTs
Feature detection settings			
threshold	Detection threshold applied to identify features	[-20K, -10K, 0K]	0.1 (day), 0.4 (night)
n_min_threshold	Minimum contiguous area required for feature detection	4000 m	0 m
position_threshold	Method for determining feature position	weighted_diff	extreme
sigma_threshold	Standard deviation for initial filtering step	3	0.5
min_distance	Minimum allowed distance between detected features	12,500 m	10,000 m
target	Whether threshold target is maxima or minima	maximum	maximum
Linking settings			
method_linking	Method used to link features	random	predict
time_cell_min	Minimum length in time that a feature must be tracked for to be considered a valid cell	600 sec	120 sec
d_max / v_max	Maximum search range (anvil) or speed (OT) at which features can move	20,000 m	100 m s^{-1}
memory	Number of timesteps a feature can vanish and still be tracked	2	2
Segmentation settings			
method	Segmentation algorithm	watershed	watershed

threshold	Threshold used for segmentation algorithm	-20 K	0.1 (day), 0.4 (night)
target	Whether threshold target is maxima or minima	maximum	maximum

The spatial distribution of OT detections is shown in Figure 1b. During the selected period of study, OTs were most frequently observed throughout the central and southern plains, along the Rocky Mountains, and across the north Atlantic storm track. To ensure that this trend was not an artifact of the transient nature of the MDS operational mode discussed above, the number of OTs in each grid box was normalized by the number of MDS observations at each grid point and plotted in Figure 1c, which confirms the spatial pattern of OTs revealed in Figure 2b. The geographic distributions are consistent with other observational OT climatologies (Cooney et al., 2018; Jellis et al., 2023).

c Statistical Analysis

To evaluate the hypothesized relationships between OT structural properties and anvil evolution, we derived storm-relative metrics describing anvil size, anvil lifetime, and the count, height, area, brightness temperature, and lifetime of OTs. A summary of the statistics and variables derived for this analysis, along with their units, are presented in Table 2. The variables in Table 2a are produced at every timestep, while the variables in Table 2b are tracked feature level life cycle variables, produced for each anvil (tracked_family_id) and OT (cell), respectively.

Table 2. Description of variables in the anvil and OT datasets. (a) Per-timestep variables recorded at each timestep. (b) Per-feature summary statistics aggregated over each tracked object's lifetime. * Indicates that the OT variable's mean was also calculated for each tracked family ID.

(a) Instantaneous (per-timestep) tracking variables			
Variable Name	**Dataset**	**Units**	**Description**
time	Anvils, OTs	UTC	Observation time
longitude	Anvils, OTs	°E	Object centroid longitude
latitude	Anvils, OTs	°N	Object centroid latitude
tracked_family_id	Anvils, OTs	—	Unique anvil identifier (constant through time)
cell	OTs	—	Unique OT identifier (constant through time)
time_family	Anvils	minutes	Elapsed time since anvil initiation
time_cell	OTs	minutes	Elapsed time since OT initiation
lifetime_norm_family	Anvils	0–1	Normalized anvil lifetime (current time / total lifetime)
lifetime_norm_cell	OTs	0–1	Normalized OT lifetime (current time / total lifetime)
ncells_family	Anvils	km^2	Anvil area
ncells_ot	OTs	km^2	OT area
ncells_ot_sum	Anvils	km^2	Sum of OT area for each tracked_family_id

min_tb_family	Anvils	K	Minimum brightness temperature within anvil
mean_tb_family	Anvils	K	Mean brightness temperature of anvil
min_tb_ot	OTs	K	Minimum brightness temperature within OT
trop_temperature	OTs	K	Tropopause temperate at object centroid
trop_relative_depth	OTs	km	OT penetration depth relative to the tropopause
associated_ots	Anvils	count	Sum of OT cell IDs linked to this anvil

(b) Lifetime (per-feature) summary statistics			
Anvil Variable (tracked_family_id)	**OT Variable (cell)**	**Units**	**Description**
anvil_lifetime	ot_lifetime*	minutes	Total tracked duration
mean_anvil_area	mean_ot_area	km²	Mean area over lifetime
max_anvil_area	max_ot_area*	km²	Maximum area reached
—	ot_area_density	km² /km²	max_ot_area* /mean_anvil_area
mean_anvil_min_tb	mean_ot_min_tb	K	Mean of minimum brightness temperature
min_anvil_min_tb	min_ot_min_tb*	K	Coldest brightness temperature reached
—	mean_trop_relative_depth	km	Mean overshoot depth (OT)
—	max_trop_relative_depth*	km	Maximum overshoot penetration depth

total_associated_ots	—	count	Number of OT cell IDs linked to this anvil
—	ot_count_density	count/ km²	total_associated_ots / mean_anvil_area
total_associated_ots_above_trop	—	count	Number of OT cell IDs linked to this anvil with trop_relative_depth > 0
ot_active_duration	—	minutes	Total time anvil had ≥1 OT
ot_active_duration_above_trop	—	minutes	Total time anvil had ≥1 OT with trop_relative_depth > 0
fraction_ot_active_above_trop	—	0-1	total_associated_ots_above_trop / total_associated_ots
fraction_ot_time_above_trop	—	0–1	ot_active_duration_above_trop / ot_active_duration
time_to_first_ot	—	minutes	Time difference between anvil initiation and first OT occurrence

The lifetime of each tracked anvil and OT feature was calculated by taking the maximum of time_family and time_cell, respectively. To facilitate comparisons across storms of different durations, we also show the variation in a number of characteristics as a function as normalized lifetime, $\tau\epsilon[0,1]$ where $\tau = 0$ corresponds to the first detection of the anvil or OT tracked feature and $\tau = 1$ to the last detection.

During the segmentation step of the *tobac* workflow, area, mean brightness temperature, and minimum brightness temperature were recorded for each tracked OT and anvil feature at

each timestamp. Anvil and OT area were defined as the total number of pixels in each object and converted to km^2 using the resolution of the grid points (0.5 km $pixel^{-1}$). Mean anvil and OT area were then calculated for each tracked feature across its full lifetime. Mean minimum brightness temperature was determined in an analogous way.

Tropopause-relative OT height was calculated using the following rearranged form (Eq. 1) of Equation 1 provided in Griffin et al. (2016), such that the height variables are on the left and the known variables from the *tobac* workflow are on the right:

$$z\_OT - z\_TP = \frac{t\_OT - t\_TP}{\Gamma\_OT} \qquad (1)$$

where z_OT-z_TP is the tropopause-relative OT height {trop_realtive_depth}, t_OT is minimum brightness temperature within the OT {min_ot_tb}; t_TP is the temperature of the tropopause {trop_temperature}; and Γ_OT is the OT lapse rate. The average lapse rate across 111 CloudSat OTs was found to be 7.34 K km^{-1} (Griffin et al., 2016), and this value was used for the current analysis. Tropopause-relative OT height and OT height are used interchangeably in the remainder of the paper.

To evaluate the relationships between OT properties and anvil evolution, the latitude and longitude of each OT were matched to each anvil mask area and assigned the corresponding tracked family ID of that anvil at each timestep. The result of this approach is two separate datasets for anvils and OTs respectively, each with tracked feature centroid locations, time, and statistics, and a common family ID to match them.

The general distributions of each feature were analyzed with simple frequency histograms plotting average OT area {mean_ot_area}, average anvil area {mean_anvil_area,

total number of OTs associated with each anvil {total_associated_ots}, minimum OT brightness temperature {min_ot_min_tb}, and OT height {max_trop_relative_depth}. The ratio of OT area to anvil area was defined as the average sum of OT area per anvil (mean of {ncells_ot_sum}) divided by the maximum area of that anvil {max_anvil_area}. To assess feature counts over the diurnal cycle, time was binned into 24 one-hour groups and unique OTs (cells) and anvils (tracked_family_id) were summed in each bin.

This study was motivated by the desire to assess relationships between OT properties that could be used to infer whether these properties are controlled by updraft strength (e.g. size, speed) or the storm's environment (e.g. stratospheric stability). Linear regression and Pearson correlation coefficient were used on OT properties aggregated across families to facilitate this (see starred (*) variables in Table 2b). Additionally, the evolution of minimum brightness temperature over normalized OT lifetime {lifetime_norm_cell} was investigated as a potential indicator of OT oscillations and usefulness for potential nowcasting applications.

To assess how OTs evolve relative to the life cycle of their parent anvils, instantaneous (per-timestep) variables from Table 2a including anvil area {ncells_family}, minimum anvil brightness temperature {min_tb_family},the sum of tracked OTs {associated_ots}, and tropopause-relative OT height {trop_relative_depth}, were averaged across normalized anvil lifetime {lifetime_norm_family}, and divided into 10 bins.

Pairwise relationships were examined by computing 2-D histograms representing the conditional distributions for six OT properties (count {total_associated_ots}, lifetime, height, area, count density, and area density) against anvil area and anvil lifetime to assess relationships between anvils and OTs. If an OT (and hence by implication, updraft) is larger in area, or sustained for a longer amount of time, then the associated CMF should result in a

correspondingly larger or longer-lived anvil, for example. Anvil area {mean_anvil_area} and anvil lifetime {anvil_lifetime} in this context refer to the lifetime (per-feature) level variables in Table 2b, where mean_anvil_area is the mean of ncells_family and anvil_lifetime is the maximum of time_family. OT properties including lifetime (ot_lifetime*}, area {max_ot_area*}, and height {max_trop_relative_depth*} were calculated as a mean for each tracked_family_id. OT count density {ot_count_density} and OT area density {ot_area_density} were defined as the total_associated_ots divided by mean_anvil_area and max_ot_area* divided by mean_anvil_area, respectively. Within each OT bin (the widths of which are dependent on the parameter of interest), 5th–95th percentile curves were calculated, with bootstrap resampling (n=300) used to estimate confidence intervals on the median curve. Log-linear regression of this median relationship was chosen to quantify scaling behavior because of the range of anvil area values. The Pearson correlation coefficient (r) and linear regression slope (β) were used to quantify the strength of each relationship through the following:

$$log_{10}(Y_{Anvil}) = \beta X_{OT} \qquad \text{(Eq. 2)}$$

Eq 2. can be rearranged to solve for the percent change in some anvil variable:

$$\Delta Y_{Anvil}\% = \left(10^{\beta X_{OT}} - 1\right) * 100\% \qquad \text{(Eq. 3)}$$

Lastly, anvil lifetime was separated into growing, mature, and dissipating stages based on the inflection points of maximum area and minimum brightness temperature following Takahashi & Luo (2014), with the goal of understanding the evolution of these storm properties

as a function of stage in storm life cycle. Of particular interest to this work is when, and for how long, OTs are active within each storm system. Variables including the time difference between anvil initiation and first OT occurrence {time_to_first_ot}, the number of OT cell IDs linked to an anvil {total_associated_ots}, and the total time an anvil had ≥1 OT {ot_active_duration}, were calculated for each storm to answer these questions. The cumulative distribution function (CDF) of ot_active_duration was also stratified by the number of OT cell IDs linked to an anvil with trop_relative_depth > 0 { total_associated_ots_above_trop} divided by total_associated_ots {fraction_ot_active_above_trop}, and the total time an anvil had ≥1 OT with trop_relative_depth > 0 { ot_active_duration_above_trop} divided by ot_active_duration {fraction_ot_time_above_trop} to gain insights in STE implications related to the total time OTs spend overshooting.

d Post Processing

Throughout the workflow, additional measures were taken to ensure the continuity of anvil and OT tracks and hence preserve accurate storm-relative statistics. First, the linking parameter *memory* in *tobac* (Table 1) was set to avoid tracking interruptions when an observation was temporarily missing, or if a feature briefly (1-2 timesteps) fell below the defined feature identification threshold. By default, *tobac* retains a unique ID through *memory*, but does not backfill the 'missing' timestep in the dataset. The absence of missing timesteps results in no statistics being generated at that time and potential relabeling of the tracked family ID due to interrupted tracking. To preserve continuity, missing timesteps were reconstructed immediately after tracking by interpolating centroid positions from adjacent frames prior to segmentation.

After segmentation statistics were calculated, all anvil objects with an area of 0 pixels were removed.

The QC process for the OTs addressed invalid family IDs. OTs are assigned a family of 0 if they are not located in an area with an identified anvil, and -1 if there is missing anvil segmentation at that time. OTs assigned only 0 or −1 throughout their lifetime were discarded. For transient 0 assignments followed by valid IDs, the 0 ID timesteps were reassigned to the first non-zero family ID. For -1 assignments, neighboring timesteps were evaluated. If adjacent IDs were consistent and non-zero, then the -1 ID was replaced with the adjacent ID accordingly. If the adjacent IDs disagreed, the local majority within ±2 timesteps was used. If a -1 ID occurred at the beginning or end of an OT lifetime and the nearest valid ID was non-zero, it was replaced with that value. At the end of this cleaning process, all OT entries retained valid tracked family IDs present in the anvil data frame.

2.3 Results

a General OT and Anvil Frequency Distributions

Basic statistics describing the general distributions of OTs and anvils in the database are listed in Table 3. The full dataset contains 292,186 OTs and 61,219 anvil families for the time period extending from March to August for years 2022-2025. Of these, 15,558 anvils were associated with at least one OT, representing just over 25% of the anvils in the database. This implies that the majority of anvils are not associated with OTs, as identified by the OT algorithm. OT-containing anvils contain approximately 20 OTs on average throughout their lifetimes, although the median value is 4 OTs per anvil. The highly skewed distribution of OTs per anvil indicates that while most anvils are associated with relatively few OTs, a small subset of large,

long-lived anvil systems are associated with a disproportionately large numbers of overshoots. As is evident from Table 3, the mean OT lifetime is ~8.5 min, and the maximum OT lifetime is ~2 h. This result supports the values of OT lifetime reported in Jellis et al. (2023). The mean anvil family lifetime is ~63.3 min, with the maximum lifetime associated with a long-lived MCS that was tracked for just under 24 h.

Table 3. Dataset-wide statistics for tracked anvil clouds and OTs. Shown are the values for the occurrence frequency, sizes, lifetimes, the distribution of OT production per anvil, temperature, and tropopause relative height for March to August in the years 2022 through 2025.

Category	**Metric**	**Value**
Summary	*Total anvils*	61,231
	Total OTs	292, 219
	Anvils associated with OTs	15,560
	Fraction of anvils associated with OTs	25.41%
Average Diameter (km)	*OTs*	6.21
	Anvils	117.25
Lifetime (minutes)	*OTs – Mean*	8.5
	OTs – Max	180.0
	Anvils – Mean	63.3
	Anvils – Max	1424.0
OTs per Anvil	*Mean*	20
	Median	4
	Mode	1
OT Brightness Temp. (K)	*Mean*	203.84

	Min	178.81
OT Trop. Rel. Height (km)	*Min*	-2.60
	Mean	0.33
	Max	3.08

General frequency distributions of various OTs and anvil characteristics are presented in Figure 4. OTs are substantially smaller than anvils, with an average diameter of approximately 5% of the mean anvil diameter (Figure 4a, Table 3). Figure 4b shows the ratio of the average sum of OT area per anvil to maximum anvil area. Most values lie between 0.1% and 1%, a result that is consistent with previous work (Itterly et al., 2025).

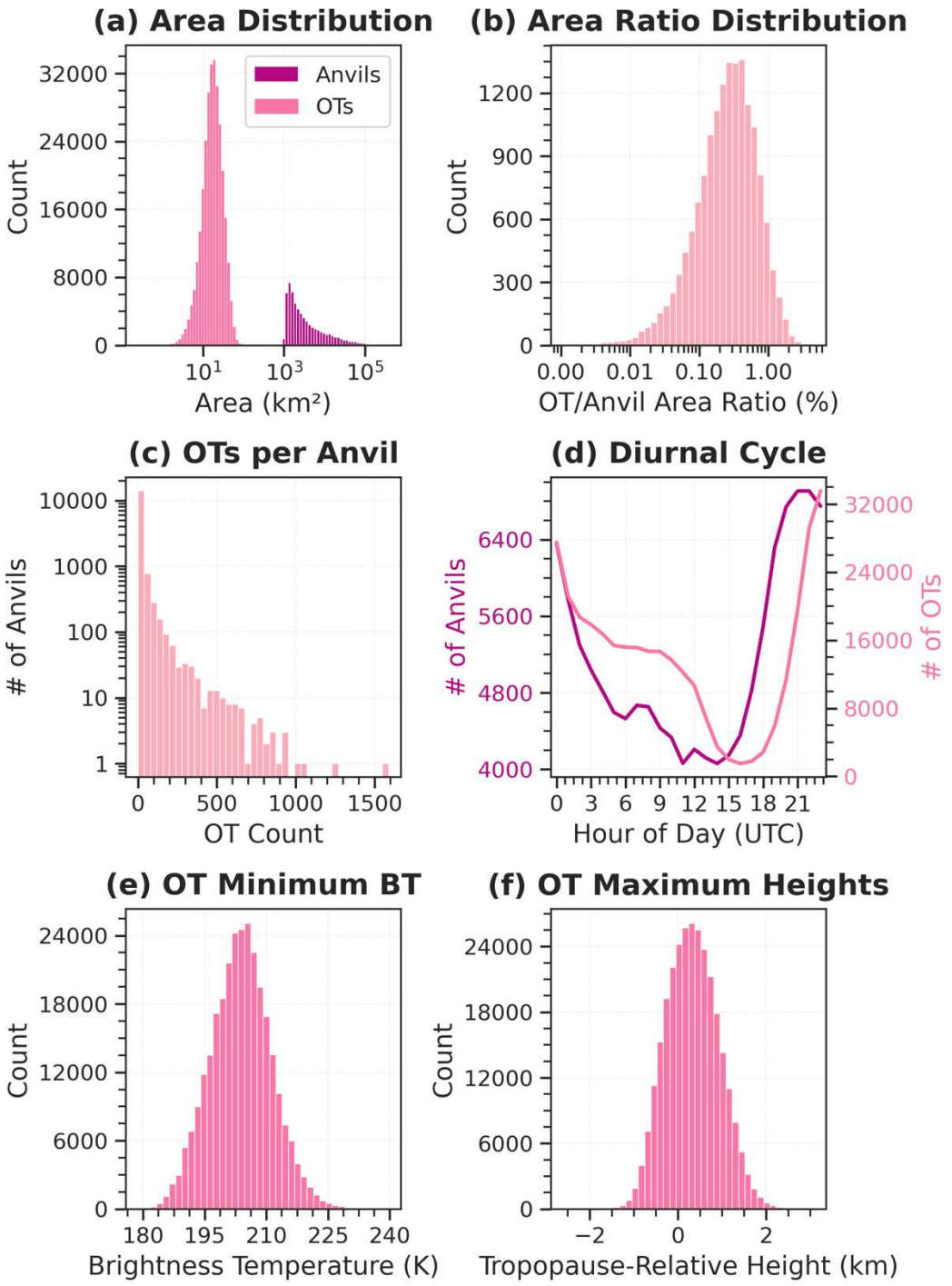

Figure 4. Frequency distributions of various anvil and OT characteristics. (a) Average anvil (purple) and OT (pink) area (km^2). (b) The ratio of the average sum of OT area per anvil to maximum anvil area (%). (c) Total OT count per anvil. (d) Average diurnal cycle of anvil (purple) and OT (pink) frequency; time expressed in UTC. (e) OT minimum brightness temperature (K). (f) Maximum tropopause-relative OT height (km).

The diurnal cycle of OTs and anvils is shown in Figure 4d. Both frequencies increase from their minimum near local noon (~17 UTC), peak in the late afternoon (20 UTC), and decrease overnight into the early morning hours. Despite both diurnal cycles in frequency taking on a similar trend, there are key differences worth noting. The OT diurnal minimum frequency occurs approximately 4 h later than the anvil minimum frequency, and the OT maximum frequency occurs about 2 h later than the anvil maximum frequency. Given the implicit assumption that OTs are driven by updraft intensity and associated CMF, and that updrafts and CMF drive anvils, this phase shift may be counter intuitive. We posit that storms may only need a few updrafts (and hence OTs) to develop anvil cloud initially, but that such storms can contain many OTs per anvil later in the day, particularly in their more mature stages, resulting in a shifted peak of OT frequency. Additionally, the number of OTs does not decrease into the morning hours as quickly as anvil counts do. In fact, OT counts stall near 06-09 UTC where a secondary increase in anvil count is evident, potentially reflecting the presence of organized nocturnal convection.

The average minimum brightness temperature of all OTs is 204 K (Figure 4e, Table 3). The distribution of tropopause-relative OT height ranges from -2.60 km to 3.08 km, with a mean of ~0.33 km above the tropopause (Figure 4f, Table 3). As such, more than 50% of all OTs exhibit positive tropopause-relative heights, implying frequent penetration into the lower stratosphere, with important implications for STE (as discussed below).

b Relationships between Various OT Characteristics

The purpose of this section is to investigate how OT properties (size, height, lifetime, and temperature) are related to each other and what these relationships imply about the updrafts that

produce them. Figure 5 shows the Pearson correlation matrix for these OT properties. OT height demonstrates the strongest overall correlations with the other OT properties, whereas OT lifetime shows the weakest associations. Here we focus on the four strongest relationships: OT height versus OT BT, OT height versus OT area, OT height versus OT lifetime, and OT area versus OT BT (Figure 6).

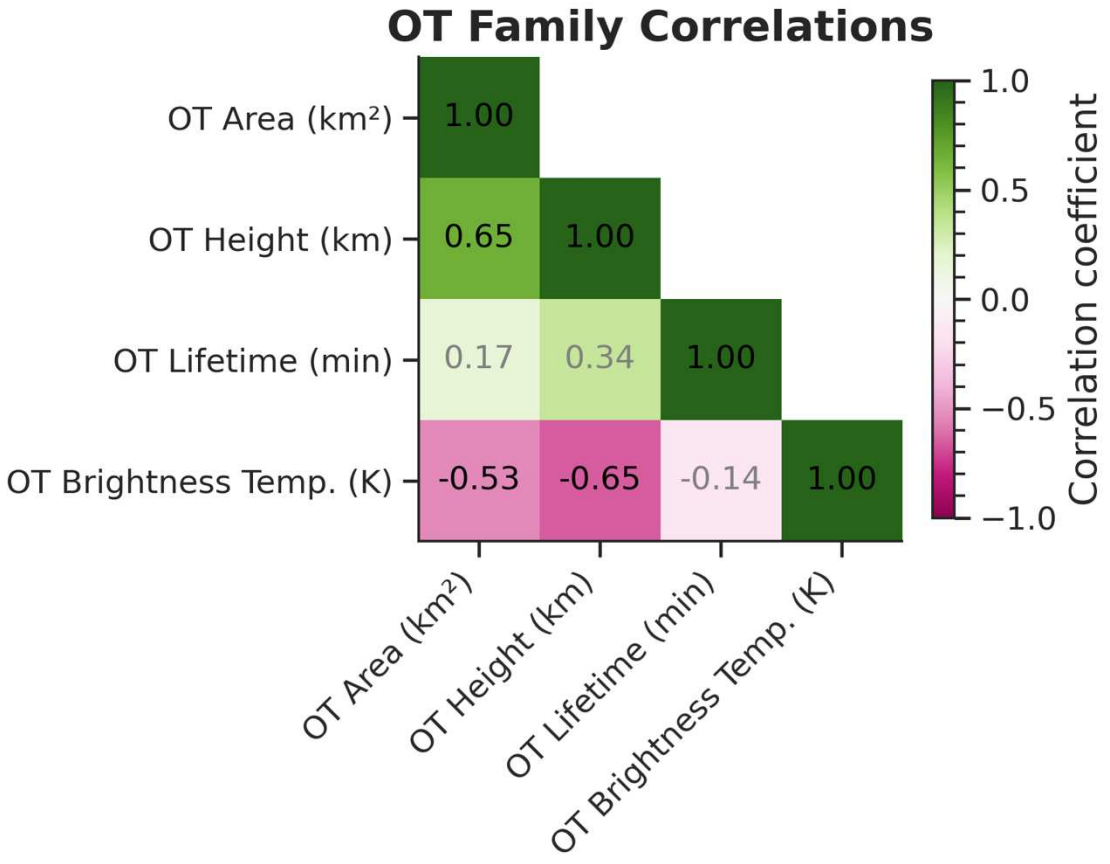

Figure 5. Correlation matrix of select OT properties shows that OT height, temperature, and area have the strongest relationships with each other. Boxes are colored by Pearson correlation coefficient (r), and values less than 0.5 are denoted with grey text.

Figure 6a shows the expected relationship between OT height and OT BT (r=-0.665). In general, taller OTs are colder, consistent with stronger updrafts penetrating higher into the atmosphere. Even OTs that penetrate deep into the stratosphere will be colder at cloud top than

lower-altitude OTs because the air within the updraft follows a near-adiabatic lapse rate rather than the surrounding environmental profile (Luo et al., 2008). There is a noticeable gap in data coverage along the diagonal between ~4 km and ~220 K. This reflects a bimodal distribution of tropical and midlatitude convection associated with the position of the subtropical jet and resulting tropopause break (not shown).

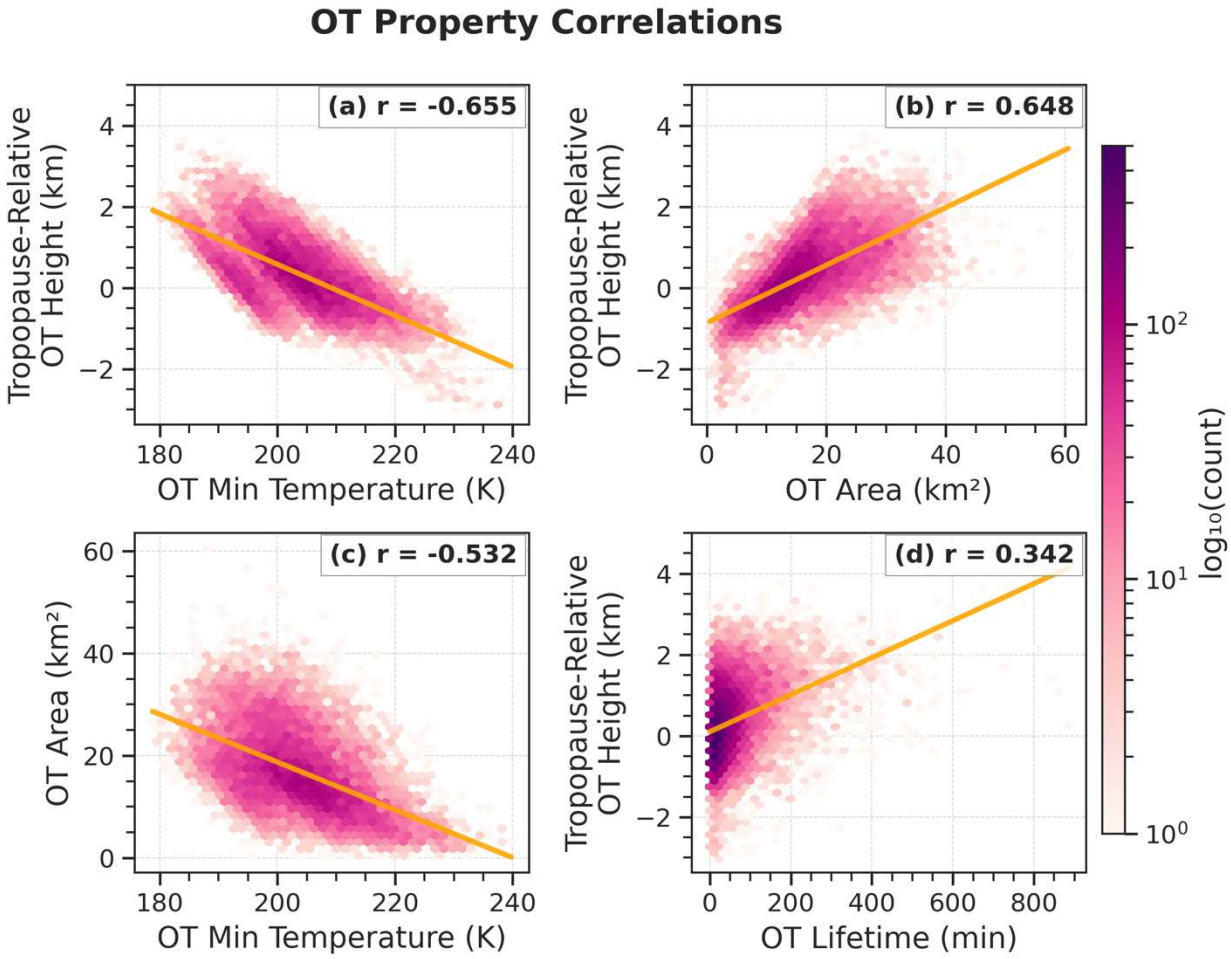

Figure 6. 2D-histgrams distributions of select OT property relationships show that OT height, temperature, and area are relatively strongly correlated. Colors indicate data density on a logarithmic scale. Pearson correlation coefficient (r) is shown for each relationship, and the linear regression is plotted in orange.

Tropopause-relative OT height is also moderately correlated (r=0.648) with OT area (Figure 6b). Although there is a cluster of very small, shallow OTs, the dominant trend shows

increasing OT area with increasing height above the tropopause, with greater spread in this relationship at larger OT areas. This behavior suggests that wider updrafts are more effective at penetrating the tropopause, thereby supporting taller OTs relative to the tropopause. It also demonstrates that wide but shallow OTs are relatively rare. Given the relationships between OT height and area, and between OT height and OT BT, it follows that OT area and brightness temperature are inversely related (r=-0.532), such that smaller (and thus lower) OTs are warmer (Figure 6c).

Figure 6d shows a positive, albeit weak, relationship between OT height and lifetime (r=0.342). The large spread in OT heights at short lifetimes, which is most common in this dataset, indicates that OT lifetime is only weakly controlled by other OT properties. This result suggests that environmental factors such as UTLS static stability or wind shear may play a more important role in determining OT persistence than updraft size alone.

Finally, we focus on the temporal evolution of OT brightness temperature given its implications for the nowcasting of extreme weather. Past studies have demonstrated that brightness temperature can be used to identify OT 'pulses' or oscillations and have even tried to correlate the number of pulses with severe weather occurrences (Borque et al., 2020). The average detrended evolution of OT brightness temperature over normalized OT lifetime is shown in Figure 7, as well as 1,000 randomly selected OT time series for comparison. While the evolution of individual OTs is highly variable, the ensemble-mean trend is small, ranging from -0.5 K to +0.5 K over the lifetime of an average OT, with slightly warmer values at the beginning and end of the OT lifetime, and cooler temperatures near mid-lifetime. Although previous work has shown that changes in OT brightness temperature and cloud top cooling can indicate storm updraft intensification (Hartung et al., 2013; Mecikalski et al., 2021), the weak signal here

suggest that brightness temperature changes alone may not be representative of changes in updraft intensity. The weak mean signal presented here may be the result of averaging over the large number of OTs in the database across a wide variety of storm environments, storm modes, OT lifetimes, etc., all of which could be hiding stronger signals present in individual cases. Higher-temporal-resolution or case study analysis may be needed to isolate pulse behavior for nowcasting. Nevertheless, the OT brightness temperature evolution of being coldest at the middle of the OT lifetime is clearly evident and in keeping with previous findings (Bluestein et al., 2019; Proud & Bachmeier, 2021)

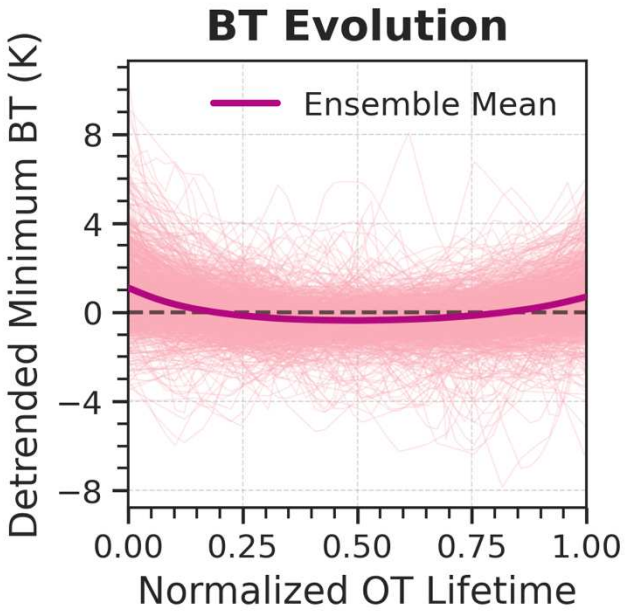

Figure 7. Average minimum OT BT subtracted from the mean (detrended) and binned across normalized OT lifetime shows a distinct U-shaped trend. The evolution of 1,000 random OTs is plotted in pink, and the ensemble average is plotted in purple.

c Anvil Characteristics

A guiding assumption for this work is if OTs serve as a proxy for updraft strength, and updraft strength drives the spatial and temporal extent of anvils, then there should be a positive

relationship between OT properties (height, area, count, and lifetime) and anvil characteristics such as area or lifetime. We examine these relationships using anvil aggregates of OT properties (described in section 2.2.c) and absolute and area-normalized metrics.

We first examine how various OT properties vary with anvil area (Figure 8). The positive relationship ($r = 0.92$) between OT area and anvil area in Figure 8a indicates that larger OTs are associated with larger anvil clouds. The log-linear regression (Eq. 3) shows that for every 1 km^2 increase in mean OT area, the corresponding anvil area increases by ~3.3%. A 5 km^2 in OT area, for example, would therefore be associated with ~17.5% in anvil area, and so on. This scaling is in keeping with the interpretation that broader updraft regions detrain more mass (in an absolute sense) into the upper troposphere, resulting in enhanced anvil areas. Despite the role that OTs may play in anvil and STE dynamics, it is clear from Figure 8c that their areas are still very small compared to the areas of their parent anvils. Furthermore, larger anvils are associated with lower OT area densities ($r = -0.81$), representing the structural difference between more compact storms with small anvils and concentrated OT counts per area compared with larger anvils in which there are fewer OTs per unit anvil area (Figure 8c).

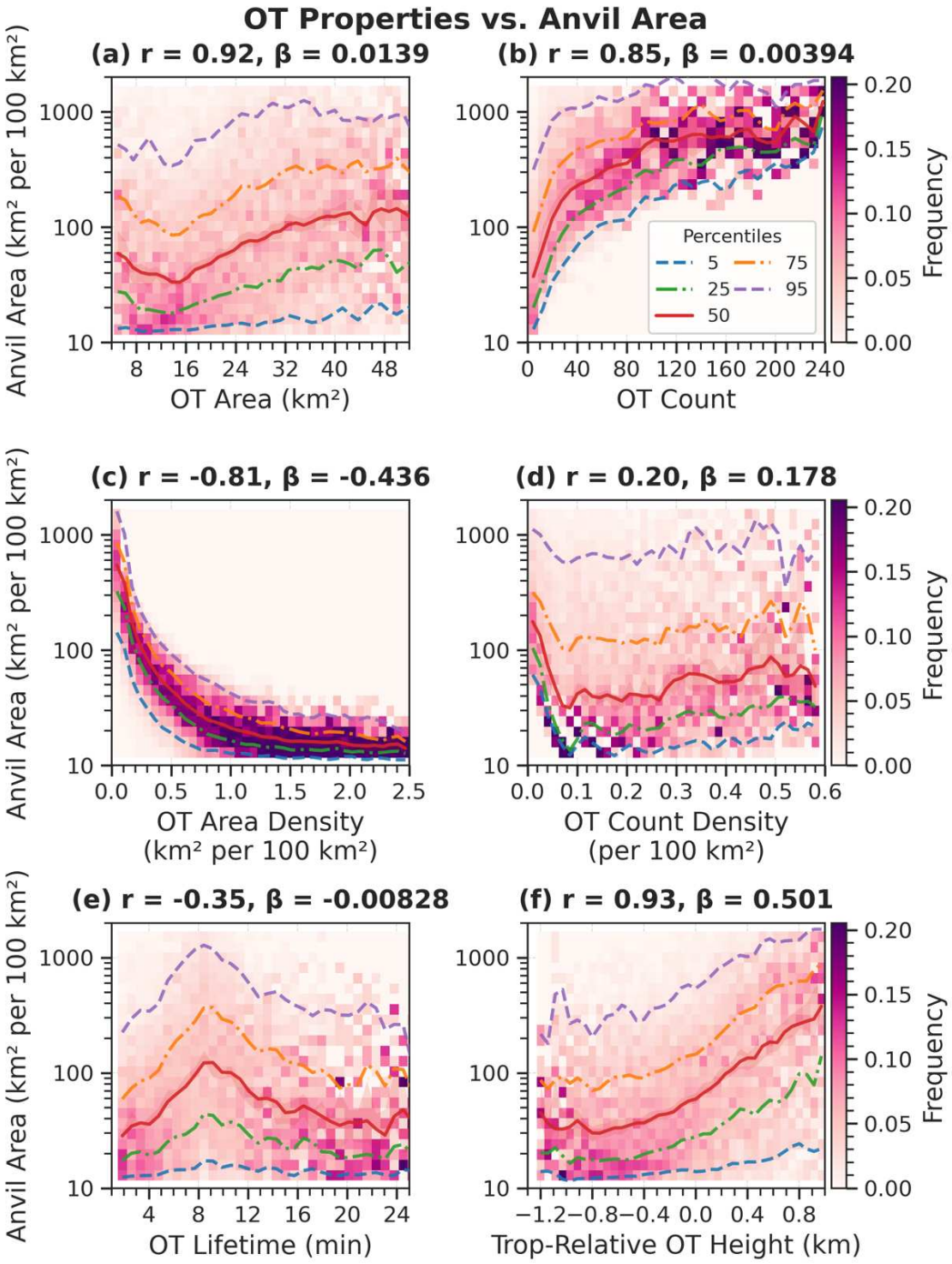

Figure 8. Relationships between various OT properties and anvil area (per 100 km^2) show that OT height and OT area density are the strongest predictors on anvil size. Various percentiles are indicated by the legend shown in panel (b). The Pearson correlation coefficient (r) and linear regression slope (β) are shown at the top of each panel for each relationship. (a) OT area (km^2), (b) OT count, (c) OT area density (km^2 per 100 km^2), (d) OT count density (number per 100 km^2), (e) OT lifetime (minutes), and (f) tropopause-relative OT height (km above the tropopause).

OT count (r =0.85) behaves in a similar way to OT area, such that a greater number of OTs is associated with larger anvil clouds (Figure 8b). While each additional OT only corresponds to a ~1% increase in anvil area, for more than 100 additional OTs, it is evident from the figure that the anvil area increases multiplicatively by 2.5x (150%). However, Figure 8d reveals that OT count density does not strongly scale with anvil size (r=0.20). Interpreting these two relationships together means that although storms with more OTs are associated with larger anvils, they do not contain more OTs per unit area. This suggests that the anvil area growth occurs more rapidly than does OT count density, as well as the fact that there may be other processes governing anvil spreading in addition to the number of deep convective updrafts (and hence OTs).

There is a weak relationship (r = -0.35) between OT lifetime and anvil area (Figure 8e), such that every 1 minute of OT lifetime is associated with ~1.8% decrease in anvil area. Overall, this implies, although weakly, that longer-lived OTs are not associated with larger anvils, and that the duration of OT events is not a primary control on anvil size. Together with the result from Figure 8b, this suggests that small, but intense storms are able to sustain persistent OTs, while storms with large anvils contain more numerous, shorter-lived OTs.

Finally, the strongest correlation is found in Figure 8f (r= 0.93), which relates OT height to anvil area. Storms with OTs that penetrate higher above the tropopause are associated with much larger anvils. For every 1 km increase in OT height above the tropopause, anvil area increases by 2.3x (130%). OT height shows the strongest correlation and regression slope of all the OT metrics (consistent with Figure 5), indicating that convective depth exerts the dominant control on anvil extent. Deeper penetrations into the stratosphere are most likely associated with

stronger updraft velocities and larger convective mass flux, both of which are likely to enhance detrainment into the upper troposphere, thereby supporting broader anvil development.

The results from Figure 8 therefore suggest that deep and large OTs, and thus deep and wide updrafts by implication, appear to be particularly effective at generating extensive anvil clouds. Although variability in OT height increases at larger anvil sizes, the consistent dominance of OT height across percentile ranges demonstrates that the height and areal extent of the OT (updraft footprint) matter more for anvil size than the OT duration or spatial density.

Figure 9 displays the relationships between OT properties and anvil lifetime. There is a positive relationship ($r= 0.68$) between OT area and anvil lifetime (Figure 9a), but only a 1% increase in lifetime per 1 km^2 increase in OT area. There is a stronger correlation ($r =0.87$) between total OT count and anvil lifetime, with larger numbers of OT being strongly correlated with longer anvil lifetimes. While one might be tempted to claim that greater numbers of OTs drive longer anvil lifetimes through enhanced CMF to the upper troposphere, such cause and effect information is not contained in this relationship and hence one should be careful in drawing such casual conclusions. All that can be stated is that longer anvil lifetimes are associated with larger numbers of OTs.

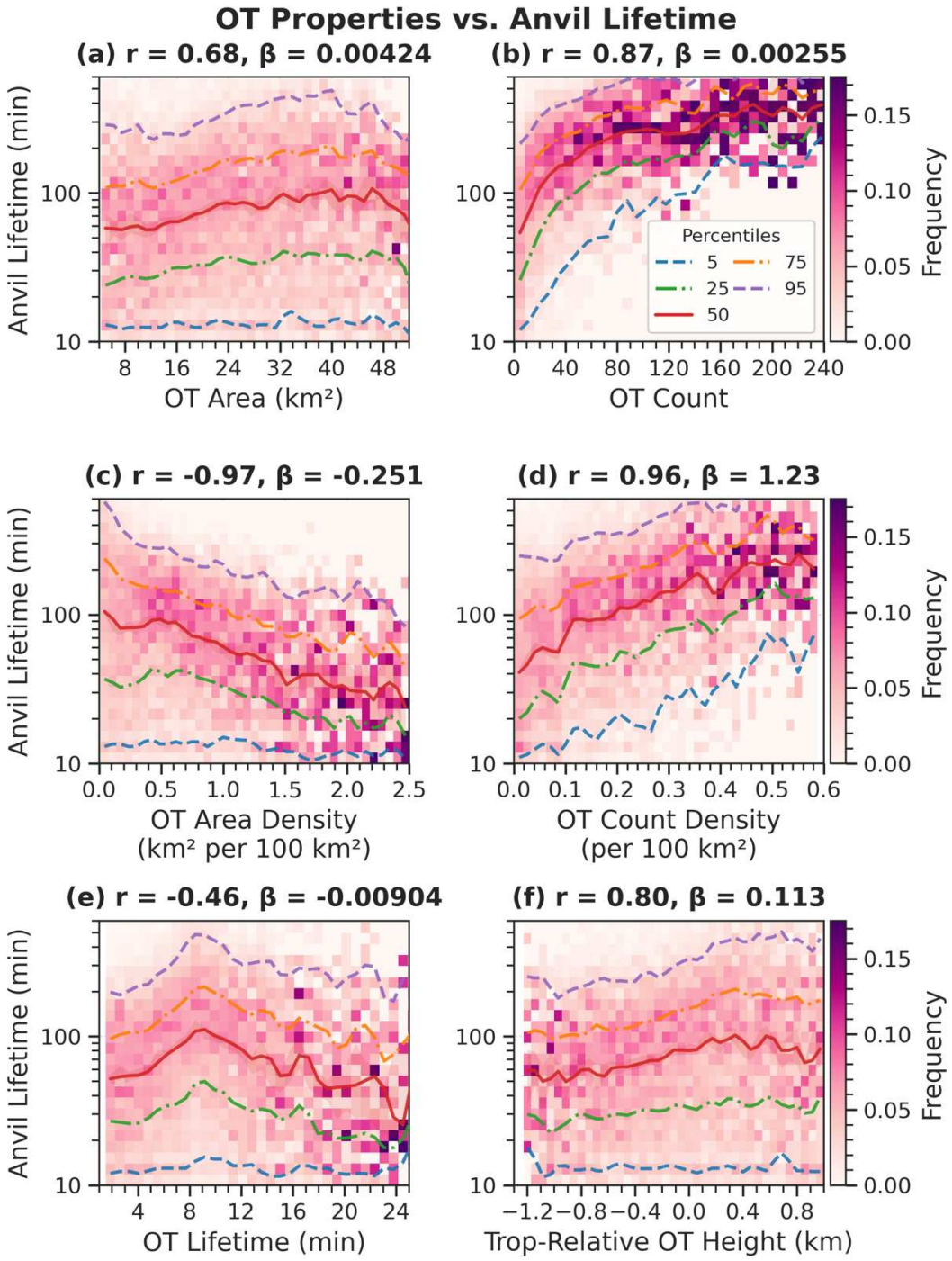

Figure 9. Relationships between various OT properties and anvil lifetime show that OT count, OT count density, and OT area density are the strongest controls on anvil longevity. Various percentiles are indicated by the legend shown in panel (b). Pearson correlation coefficient (r) and linear regression slope (β) are shown for each relationship. The figures show the relationship between anvil lifetime and (a) OT area (km^2), (b) OT count (number), (c) OT area density (km^2 per 100 km^2), (d) OT count density (number per 100 km^2), (e) OT lifetime (minutes), and (f) Tropopause-relative OT height (km above the tropopause).

Similar to the results show in Figure 8, there is a negative relationship between OT area density and anvil lifetime (Figure 9c). Greater OT area density strongly correlates (r=-0.97) with shorter anvil lifetimes, such that for every additional unit of OT area density, anvil lifetime decreases by 44%. Conversely, Figure 9d shows a per unit increase in OT count density scales with area lifetime by +17.7x (1,670%), and that this relationship is very strong (r = 0.96). While OT count density was not associated with a meaningful impact on anvil area (Figure 9d), it does appear to be strongly linked to anvil longevity, highlighting that anvil size and anvil lifetime capture different aspects of storm evolution. Again, we see that there is weak to moderate negative correlation between OT lifetime and anvil lifetime (r = -0.46), wherein a 1-minute increase in OT lifetime corresponds to 1.7% decrease of anvil lifetime (Figure 9e).

There is also a moderate relationship (r=0.80) between OT height and anvil lifetime (Figure 9f). Similar to the positive relationship between OT height and anvil area, anvils associated with deeper overshoots persist longer, with a 30% increase in anvil lifetime per 1 km of penetration above the tropopause. Overall, these results indicate that anvil lifetime is more closely associated with convective depth and spatial density of OTs than with the duration of individual overshooting events.

d Life Cycle Analysis

As described above, the use of *tobac*'s family tracking resulted in a unique dataset that provides information about anvils over their complete life cycle. We used these tracked families to composite anvil and OT properties across the full lifetime of each anvil.

It is clear from Figure 10a that lifetime-normalized anvil area and anvil brightness temperature evolve inversely from one another. Anvil area slowly increases to a maximum

around 55% of the anvil lifetime ($\tau \approx 0.55$) before tapering off again, while brightness temperature reaches its coldest values near $\tau \approx 0.3$ and then warms approximately monotonically through the end of the lifecycle ($\tau = 1$). These inflection points in area and brightness temperature have been used by Takahashi and Luo (2014) to indicate the 3 life cycle stages of storms: growing, mature, and dissipating, and are marked in Figure 10a for reference. The anvils in this database spend most of their time (45%) in the dissipating stage, which is consistent with those anvils observed by CloudSat (Takahashi & Luo, 2014).

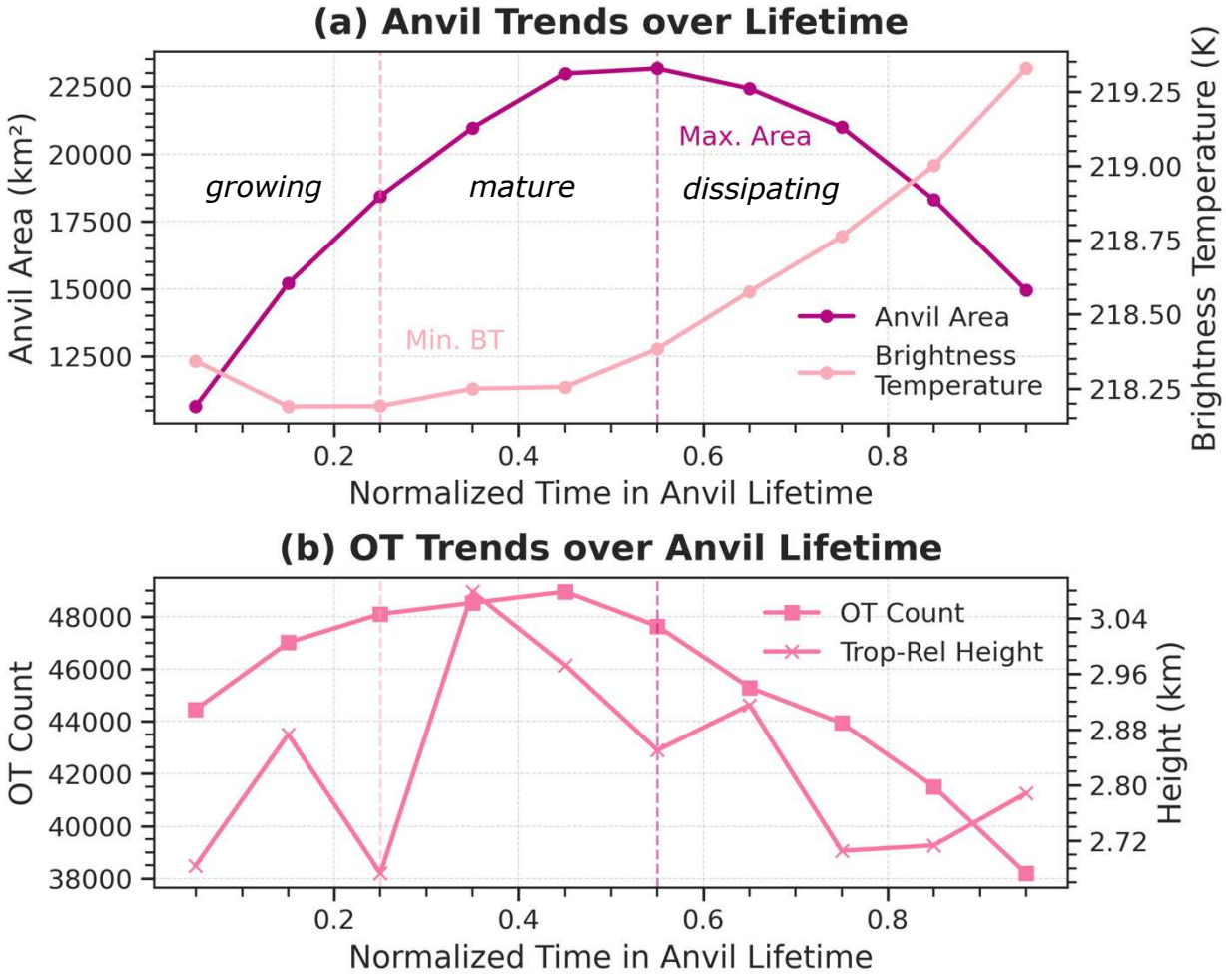

Figure 10. Anvil and OT trends over the normalized lifetime of the anvil area show that OT count and OT height peak during the mature stage of anvil lifetime. (a) Average anvil area

(purple) and minimum anvil BT (pink) over the normalized anvil lifetime. (b) OT count (squares) and maximum OT height (crosses) over normalized anvil lifetime. Maximum area and minimum BT are marked to denote growing, mature, and dissipating stages as defined by Takahashi and Luo, 2014.

Figure 10b shows how OT count and OT tropopause-relative height evolve over normalized anvil lifetimes. The OT count reaches a maximum during the mature stage of the anvil and subsequently decreases to an absolute minimum through the remainder of the life cycle. This indicates that overshooting is more frequent and deeper in the developing and mature phases of the anvil life cycle, than during the time periods when the anvil is dissipating. This is consistent with the interpretation of Figure 4d, which implies that only a few OTs are needed to enhance anvil growth at initiation, but that the number of OTs is highest during the mature stage when convection/updrafts become more organized. As anvil area is strongly impacted by storm life cycle, this suggests that OT density per anvil area is also influenced by anvil life cycle, a trend already demonstrated in Figure 8c.

Figure 10b shows that OT height varies throughout anvil lifetime, is indicative of pulses or oscillations around the LNB, and is consistent with intermittency in overshoot depth through time. The maximum OT height occurs during the mature stage of the anvil. This indicates that the deepest overshoots coincide with the period of the greatest OT frequency.

The relatively consistent phase shifts between anvil evolution and OT properties suggests that overshooting behavior evolves in lockstep with the storm anvil throughout the storm life cycle stages. The early occurrence of the coldest anvil cloud-top temperatures suggests fast vertical growth and strong updrafts characteristic of the developing storm stage. An increase in overshooting frequency and variations in tropopause-relative OT height during this stage reflects multiple convective pulses within a growing storm complex. The peak in OT count and height

during the mature stage is consistent with a transition to strong, potentially-more organized, deep convection. As the anvil area expands and stratiform regions start to dominate, the environment near the tropopause is influenced by changing static stability, gravity wave activity, or mesoscale organization, and appears to continue to support strong, intermittent OT penetrations. Overall, this paints a picture of a shift from many moderate OT penetrations during the early growth of the storm system, to less frequent 'pulses' of deep convection in the mature phase of storm life cycle. These pulses of deep convection assist in driving the enhanced areal development of the anvil and may be influenced by turbulence at anvil top.

Figure 11 summarizes the behavior of anvils regarding OT occurrence. The time difference in minutes between the start time of each identified anvil and the first OT to be identified within each anvil is plotted in Figure 11a. The most common time difference between OT and anvil identification is within 10 minutes before *and* after the start of anvil development. The negative time differences between the start time of each anvil and the time an OT is first identified and associated with an anvil is an interesting result. A subset of the distribution in Figure 11a fall below zero, implying that an OT is detected before the associated anvil family is detected. Two mechanisms may explain this behavior.

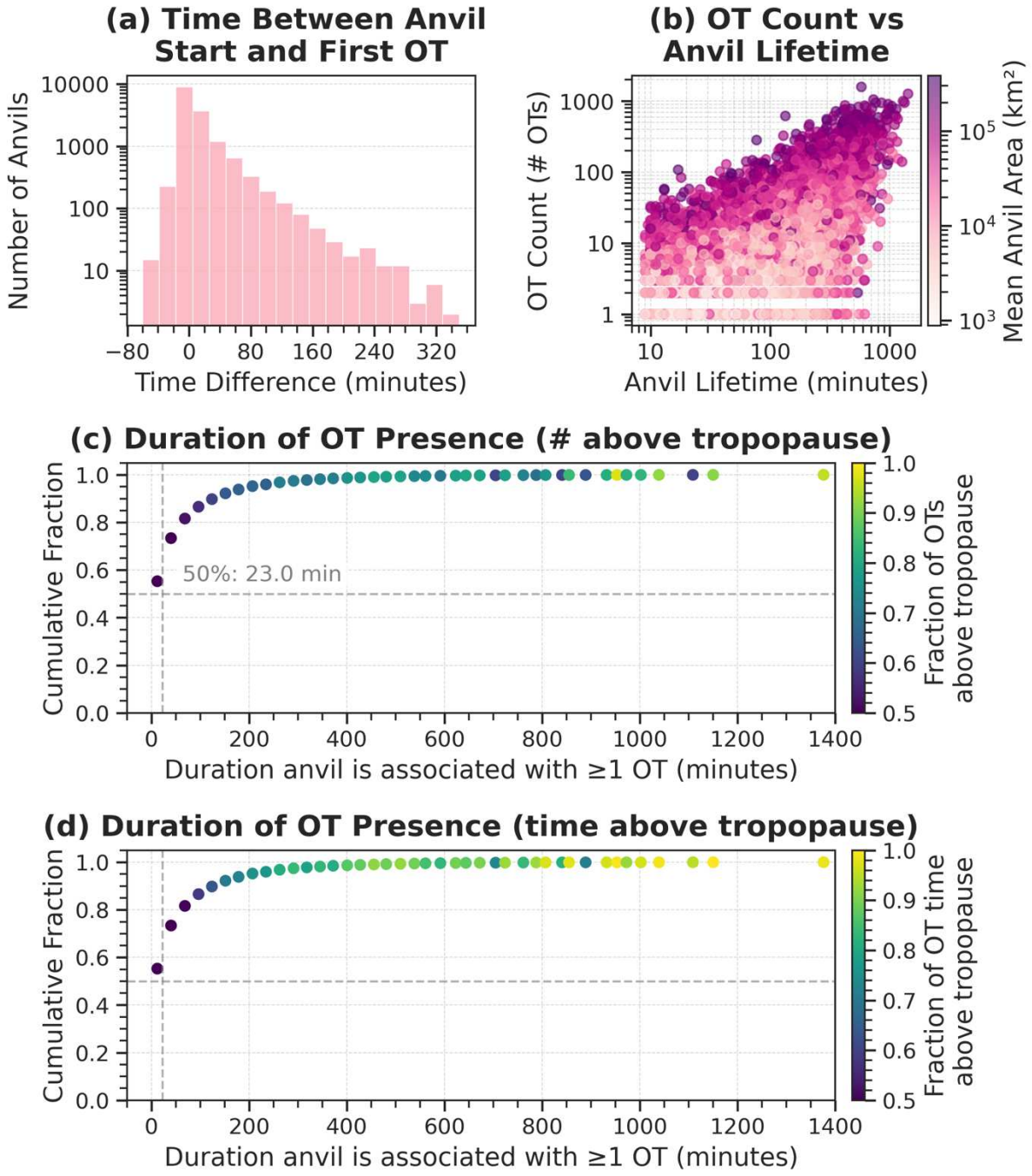

Figure 11. Summary of first OT occurrences and total OT occurrence time for each anvil shows that the presence of OTs is related to anvil initiation time and total anvil lifetime. (a) Frequency histogram distribution of the time difference (minutes) between the first anvil identification time and the time an OT is first associated with each anvil, binned every 20 minutes. (b) anvil lifetime (minutes) and OT count colored by the mean anvil area (km^2). (c) CDF of the duration of total OT presence for each anvil colored by the fraction of OT counts above the tropopause. (d) CDF of the duration of total OT production for each anvil colored by the fraction of time OTs spent above the tropopause.

First, there are differences in detection sensitivities between OT and anvil segmentation thresholds. The OT detection algorithm is optimized to identify localized, anomalously cold pixels relative to the surrounding anvil cloud, whereas *tobac* anvil segmentation requires a contiguous region exceeding a BTD threshold. As a result, a compact but intense overshooting updraft embedded within developing convection may satisfy the ML model's criteria before the surrounding anvil cloud expands sufficiently to meet the *tobac* tracking and segmentation thresholds. While the post-processing step described in section 2.2.d was implemented to minimize these tracking artifacts, small timing offsets may still occur near detection thresholds. Additionally, these offsets appear to be concentrated within ±10 minutes of anvil initiation and thus, the authors argue, are small relative to storm evolution timescales (mean lifetime > 60 min).

Alternatively, this behavior may suggest that at least some of the negative time differences between anvil start time and the time an anvil is first associated with an OT represent physical storm development processes rather than algorithmic artifacts. Strong updrafts in certain environments may initially develop rapidly in the vertical direction before sufficient detrainment produces a detectable anvil, thereby generating OT signatures prior to the formation of an extensive anvil shield. Negative time differences between OT and anvil identification occur in ~18% of anvils containing OTs, indicating that while this trend is not dominant in OT-anvil relationships, it does occur in a measurable subset of storms. Regardless of the mechanism in play, the narrow distribution of differences centered near zero suggest that the presence of an OT is tightly coupled to anvil initiation in these observations, even if OT frequency peaks later in the anvil life cycle (Figure 10b).

Total OT occurrence generally increases with total anvil lifetime (Figure 11b). Consistent with this scaling, longer-lived anvils are associated with larger mean anvil areas and tend to be

associated with a greater number of OTs, although the spread of OT occurrences increases substantially at longer anvil lifetimes. Figures 11c and 11d show the cumulative distribution of anvils durations during which they were associated with at least one OT. These figures demonstrate that short duration events of OTs present in anvils dominate the distribution, however, that the distribution includes a long tail representing storms that frequently overshoot for extended periods of time. At least half of the anvils in the database contain at least one OT for a total of 23 minutes of their lifetime (Figure 11c). The transition in the fraction of OTs that reach above the tropopause during a storm's lifetime (as indicated by the transition from purple to green colors from left to right) increases quickly to over 80% and reaches a maximum at around 400 minutes of total anvil lifetime before becoming highly variable (Figure 11c). The storms that lie beyond 400 minutes live well past the average anvil lifetime and represent the extreme right tail of the distribution. This is consistent with the results shown above of the mean tropopause relative OT height being above zero, and thus that OTs are overshooting the tropopause more often than not.

For additional context, the identical CDF is colored instead by the amount of time for which a storm contains tropopause-overshooting convection in Figure 11d. Comparison between the two panels reveal that for the majority of storms, the fractional time that anvils have OTs that extend above the tropopause is consistently higher (>80%, indicated by more green and yellow colors) than the fractional number of OTs that reach the tropopause (<80%, indicated by more purple and blue colors). This difference suggests that although a lower fraction of OTs is reaching the stratosphere, most of the anvil lifetime is spent with OTs above the tropopause, and thus their STE impacts may be more impactful than expected.

2.4 Discussion and Conclusion

The research described in this thesis has demonstrated novel insights into the characteristics of overshooting tops and their relationships to their parent anvils. A database of storms was constructed using GOES-East data during the North American mid-latitude convective season (March-August) for 2022, 2023, 2024 and 2025. Nearly 300,000 OTs were detected with an automated ML detection model and then tracked using *tobac*, a cloud object tracker. Through this process, ~61,000 anvils were also identified, tracked, masked, and assigned a universal, temporally consistent family ID to co-locate OTs within their respective parent anvils. Of these anvils, about 25% (~15,000) were associated with at least one OT. The identified OTs have an average diameter of around 6km, and the distribution of OTs per anvil is highly skewed due to a few rare, large, long-lived storm systems whose anvils contain many OTs. Notably, the average OT lifetime (~ 8.5 min) is shorter than the current temporal resolution of global geostationary observations (~10 min).

We used the distributions of various OT and anvil characteristics to assess hypothesized relationships between OT properties (area, brightness temperature, height, and lifetime) and anvil characteristics (area and lifetime). We also assessed how these relationships vary over anvil lifetimes.

First, correlations among OT properties show that taller OTs are colder and larger than shallower OTs, consistent with the hypothesis that stronger updrafts are able to transport more mass to higher altitudes. However, our results demonstrate that OT height shows little relationship with OT lifetime, indicating that deeper OTs are not necessarily longer-lived. This suggests that other environmental controls, such as UTLS static stability and shear, may play a more important role in OT longevity than updraft strength alone.

We also analyzed the temporal evolution of OT brightness temperature to understand its potential usefulness as a proxy for changing storm intensity. On average, OTs are coldest at the middle of their lifetime, although individual OTs show substantial variability. The small mean temperature change suggests that brightness temperature evolution alone may not reliably diagnose updraft strength at these time scales, though fluctuations in individual cases may still provide information on OT pulsing behavior.

We next investigated how OT properties scale with anvil area and lifetime. OT height appears to be the most dominant scaling variable analyzed here, such that anvil size and longevity are both strongly correlated with the strength and intensity of convective updrafts. We discovered that there is no clear relationship between OT lifetime and anvil size or anvil lifetime, indicating that longevity of OTs does not strongly relate to the spatial or temporal extent of anvils. Instead, our results suggest that it is the sheer number of OTs per anvil that are associated with anvil longevity, even if the more numerous OTs are somewhat smaller in size. Meanwhile, it is the percentage of anvil area covered by OTs that is associated with larger anvils, even if those OTs are fewer in number, though this integrated OT area is not associated with anvil persistence. The results around these two regimes (longer lived storms with smaller, more numerous OTs vs larger storms with larger, less numerous OTs) may compliment previous work which found that isolated supercells exhibit larger updrafts and deeper overshoots compared to other storm modes, while MCSs have a greater number of weaker overshoots that were able to achieve more overall STE (Bigelbach et al., 2014).

Finally, we examined anvil-OT relationships over storm lifecycle by compositing OT and anvil characteristics over normalized anvil lifetime. The composite analysis suggests that anvils in this dataset spend a relatively large fraction of their normalized lifetime in the dissipating

stage, which is in agreement with previous satellite-based studies (Takahashi & Luo, 2014). OT occurrence is found to peak during the early stages of the anvil life cycle, and in some cases, OTs are even detected shortly before the parent anvil. Additionally, the evolution of OT properties is offset from anvil evolution by a consistent phase shift, which suggests that overshooting behavior evolves systematically with storm life cycle stage. The cumulative time of OT presence within anvils is dominated by short-duration events (23 minutes), with a long tail of rare storms that overshoot for extended time periods. It's important to note that the presence of OTs does not necessarily correlate one-to-one with stratospheric impact. As we showed, while a lower fraction of OTs within anvils reach the stratosphere, most of their time associated with a storm is spent above the tropopause, and thus their STE impacts may be greater than anticipated.

While a number of interesting OT, anvil, and OT-anvil relationships have been demonstrated in this study, it must be noted that the results of this study are constrained by the assumptions and thresholds used in identifying and tracking anvils and OTs. A recent update to the NASA svrstormsig ML OT detection model removed the use of the vis_tropdiff model in favor of potentially more equitable detections between day/night. The linear weighting function in the tropdiff model was also replaced with a cosine-weighted function in efforts to enhance the accuracy of consistent, true, detections. The impacts of these changes would need to be assessed within context of the current study.

Additionally, while implications for convective updrafts are suggested, no OT detection can be assumed to perfectly represent the location or intensity of an updraft without direct observations of the vertical structure of the storm. Understanding the physical processes driving OT timing relative to anvil development will require information on updraft velocity and structure, such as the observations provided by EarthCare (Illingworth et al., 2015) and the

upcoming NASA INCUS mission (van den Heever, 2021). Additionally, our findings around the controls on anvil size and lifetime highlight the potential for future work to explore OT/anvil relationships in the context of storm morphology and estimates of STE. But again, because OT size and OT height are only proxies for updraft strength, direct measurements of updraft velocity and CMF will be needed to determine which processes most strongly regulate anvil development. Field campaign measurements of convective stratospheric injections (such as DCOTSS) could also be used to calculate estimates of total convective impacts on the stratospheric water vapor budget. Finally, the incorporation of environmental variables such as wind shear, CAPE, and statistic stability could shed light on the weaker relationships (such as OT lifetime and anvil area) presented in section 2.3.

Overall, this research demonstrates systematic relationships between OT properties and the characteristics of their parent anvils and highlights the importance of OT height and hence convective depth, as well as OT count density, as the primary predictors of anvil size and lifetime. We've expanded on past work linking updraft intensity to OTs and anvils separately by showing how anvils and OTs evolve together throughout the diurnal cycle. The results have important implications for different storm mode regimes and cross-tropopause transport, specifically surrounding the fractional amount of time that an anvil's OTs spend in the stratosphere. Ultimately, we conclude that given the demonstrated relationships between OTs and anvils over anvil lifecycles that improved quantitative estimates of overshooting convection are critical for understanding anvil properties and evolution, as well as convective contributions to STE and their impacts on UTLS composition and climate.

Chapter 3 CONCLUSIONS

3.1 Summary and implications of key findings

The overarching goal of this thesis has been to answer the question: "How are OT characteristics related to the structural and temporal properties of their parent anvils?" We addressed this goal by first building separate OT and anvil databases with four years of high temporal resolution geostationary satellite data over the eastern US. Then, with the help of a novel 'tracked family' *tobac* algorithm approach, the databases were closely linked in space and time through the use of a common storm object ID, and storm level statistics were then calculated over the full evolution of OT and anvil life cycles.

The analysis of our results allowed us to draw the following conclusions addressing the five science questions laid out in chapter 1:

a *How many distinct OTs is an individual anvil associated with, and at what point in the anvil life cycle does the OT count peak?*

An individual anvil is associated with ~20 OTs on average, although the median number of OTs per anvil is only 4, and the mode is 1 OT per anvil. As such, the distribution of OTs per anvil is extremely skewed with a long right tail. The maximum number of OTs associated with an anvil was 1587. The number of OTs peaks around halfway through the anvil lifecycle (τ = 0.55), or during the mature stage of anvil life cycle. OT frequency varies diurnally, with a global maximum at ~21 UTC and a secondary local maximum between 06-09 UTC. Furthermore, this OT cycle is positively offset from the diurnal cycle of anvils by 2-4 hours (i.e., 2-4 hours later), suggesting a preference for OT frequency during the early to middle stages of anvil lifetime. The time difference between anvil start time and the first identified OT was almost always < 10

minutes, and in 20% of cases, OTs were identified 10 minutes before anvils. Thus, we concluded that the presence of OTs is tightly coupled to anvil initiation. In total, over half of the anvils observed were associated with OTs for over 20 minutes, or about 1/3 of the mean anvil lifetime. Finally, it was also evident that the fraction of OTs that existed above the tropopause was consistently larger than the fraction time OTs spent above the tropopause.

b How do OT structural characteristics (height, area, and lifetime) vary with one another?

OT structural characteristics scale weakly to moderately strongly with each other. As expected, OT height and OT brightness temperature have a strong negative relationship which is in keeping with the fact that strong updrafts are capable of transporting mass to higher altitudes and are thus observed as having colder brightness temperatures. This is also consistent with the ML detection model assumptions, as well as previous work that has identified local areas of minimum brightness temperatures are indicative of deep overshooting updrafts. OT height and OT brightness temperature are also both moderately correlated with OT area ($r = 0.65$ and $r=-0.53$, respectively) which implies that spatially larger OTs are able to ascend to greater depths above the anvil, and that they are colder as a result. Lastly, there is a weak relationship between OT height and OT lifetime, indicating that deeper OTs are not necessarily longer-lived. This suggests that other environmental controls, such as UTLS static stability and shear, may play a more important role in OT longevity that updraft strength alone.

c How does brightness temperature fluctuate throughout OT lifetime?

The evolution of brightness temperature through normalized OT lifetime takes on a U shape, where OTs start warm relative to their mean temperature at OT initiation ($\tau=0$), gradually decrease to a minimum brightness temperature near $\tau=0.5$, before warming again through $\tau=1$. The relative changes in brightness temperature during this evolution are small, ranging from -0.5

to 0.5 K. The limited magnitudinal variations are likely, at least in part, a result of averaging over many OTs in varying storm environments, different storm modes, OT lifetimes, etc. Stronger temperature variations could still be present in individual cases and may reveal information on the pulsing behavior OTs exhibit in visible satellite imagery.

d Are storms with more OTs associated with longer lived and/or larger anvils than storms with fewer OTs?

Storms with more OTs are associated with larger and longer-lived anvils than storms with fewer OTs. Both anvil area and anvil lifetime are associated with increases in OT count, by 150% and 80% respectively. However, their responses to OT count density (the number of OTs per 100 km^2 of anvil area) differ. While OT count density does not closely scale with anvil size ($r=0.20$), the relationship between OT count density and anvil lifetime is an extremely strong, positive relationship ($r=0.96$). Therefore, while larger and longer-lived anvils are closely associated with greater total numbers of OTs, increases in the temporal and/or spatial distribution of OTs throughout the anvil (i.e., OTs per unit area of anvil) are only linked to anvil longevity. Alternatively, the number of OTs per anvil does not scale linearly with anvil size.

e How do OT properties scale with anvil size and anvil lifetime?

We discovered that there is no clear scaling relationship between OT lifetime and anvil size, nor between OT lifetime and anvil lifetime. In contrast, OT area and OT height both increase with anvil area and anvil lifetime in an absolute sense, suggesting that both updraft size and updraft strength, respectively, contribute positively to anvil extent and persistence. Anvil size and anvil lifetime are both found to decrease with increasing OT area density, indicating that anvil expansion outpaces the growth rates and spatial coverage of individual overshooting updrafts. Interpreted together with the conclusions drawn in addressing science question 2, these

results are complimentary to Bigelbach et al., (2014), which found that MCSs (larger anvil shield) contain a greater number of OTs that are more sparsely distributed per anvil area, while supercells (smaller anvil shields) have more isolated updrafts (lower OT count) that are larger and overshoot higher.

As discussed in the introduction, a number of previous studies have built multi-year regional OT databases to analyze the spatial and temporal distributions of these cloud top features. Our findings contribute to this understanding by linking these OT observations to their parent anvils in space and time, and by calculating storm-scale statistics across OT and anvil life cycles. Until this research, such calculations had not been performed using the fine temporal resolution available from the GOES-East MSD. We have not only gained an understanding of where in an anvil's life cycle OT occurrence is most frequent, but also of the relevance of different OT characteristics to the spatial extent and longevity of anvils.

There are a few limitations to the conclusions presented above. First, the results of this study were constrained by the assumptions and thresholds used in identifying and tracking anvils and OTs. Such assumptions and/or thresholds may contain errors. A recent update to the NASA svrstormsig ML OT detection model removed the use of the vis_tropdiff model in favor or more equitable detections between day/night and replaced the linear weighting function in the tropdiff model with a cosine-weighted function to improve the accuracy of consistent, true, detections. The impacts of these changes would need to be assessed within context of the current study to understand how the results would change, if at all. Also, while the settings used to generate the databases presented here were tested across a range of possible values, any unique combination of these choices may result in slightly different detections. Furthermore, even if the tracking algorithm behaves exactly as expected, no OT detection can be assumed to perfectly represent

the location or intensity of an updraft without observations of the vertical structure of the storm and the updraft velocities. Finally, while previous studies have used OT height and area as a proxy for updraft strength, and while similar assumptions are utilized in this study, it is impossible to draw causality the relationships between OT characteristics and anvil evolution with the observations leveraged for this thesis.

3.2 Future work

This thesis contributes to an understanding of how OT properties are related to the characteristics and evolution of their parent anvils. The resulting analysis opens further questions about the role of updraft strength and CMF in controlling aspects of anvil evolution such as area and lifetime. The next step in the research presented here should be to determine the roll of differing storm morphologies on the spatial and temporal evolution of deep convective updrafts, and the subsequent OTs and anvil properties. Our findings seem to be consistent with the storm mode separation of OT distribution and area presented in Bigelbach et al. (2014), and highlight the potential for future work to explore OT/anvil relationships in the context of storm morphology and estimates of STE. Incorporating environmental variables such as wind shear, CAPE, and statistic stability could also shed light onto the weaker relationships that were reported, where the primary controls on anvil area or lifetime were not clear.

Additionally, since OT size and OT height are only proxies for updraft strength, direct measurements of updraft velocity and CMF are necessary to determine which processes most strongly regulate anvil development. Such observations of vertical velocity have recently become available with the launch of EarthCare. Understanding the physical processes driving OT timing relative to anvil development will require information on updraft velocity and structure, as well

as CMF, which will be provided by future missions such as the NASA INCUS mission (van den Heever, 2021) to be launched in 2027. With this fuller, 3D picture of deep convective storms, in-situ measurements of convective stratospheric injections from field campaigns such as DCOTSS could also be used to calculate estimates of total convective impacts to the stratospheric water vapor budget.

REFERENCES

Anderson, J. G., Wilmouth, D. M., Smith, J. B., & Sayres, D. S. (2012). UV Dosage Levels in Summer: Increased Risk of Ozone Loss from Convectively Injected Water Vapor. *Science*, *337*(6096), 835–839. https://doi.org/10.1126/science.1222978

Apke, J. M., Mecikalski, J. R., Bedka, K., McCaul, E. W., Homeyer, C. R., & Jewett, C. P. (2018). Relationships between Deep Convection Updraft Characteristics and Satellite-Based Super Rapid Scan Mesoscale Atmospheric Motion Vector–Derived Flow. *Monthly Weather Review*, *146*(10), 3461–3480. https://doi.org/10.1175/MWR-D-18-0119.1

Auth, R. M., & Homeyer, C. R. (2023). Targeted Balloon Observations of Stratosphere-To-Troposphere Transport From a Mesoscale Convective System. *Journal of Geophysical Research: Atmospheres*, *128*(16), e2023JD039139. https://doi.org/10.1029/2023JD039139

Bedka, K. (2011). Overshooting cloud top detections using MSG SEVIRI Infrared brightness temperatures and their relationship to severe weather over Europe. *Atmospheric Research*, *99*(2), 175–189. https://doi.org/10.1016/j.atmosres.2010.10.001

Bedka, K., & Khlopenkov, K. (2016). A Probabilistic Multispectral Pattern Recognition Method for Detection of Overshooting Cloud Tops Using Passive Satellite Imager Observations. *Journal of Applied Meteorology and Climatology*, *55*(9), 1983–2005. https://doi.org/10.1175/JAMC-D-15-0249.1

Bedka, K., Brunner, J., Dworak, R., Feltz, W., Otkin, J., & Greenwald, T. (2010). Objective Satellite-Based Detection of Overshooting Tops Using Infrared Window Channel

Brightness Temperature Gradients. *Journal of Applied Meteorology and Climatology*, *49*(2), 181–202. https://doi.org/10.1175/2009JAMC2286.1

Bedka, K., Dworak, R., Brunner, J., & Feltz, W. (2012). Validation of Satellite-Based Objective Overshooting Cloud-Top Detection Methods Using CloudSat Cloud Profiling Radar Observations. *Journal of Applied Meteorology and Climatology*, *51*(10), 1811–1822. https://doi.org/10.1175/JAMC-D-11-0131.1

Bedka, K., Wang, C., Rogers, R., Carey, L. D., Feltz, W., & Kanak, J. (2015). Examining Deep Convective Cloud Evolution Using Total Lightning, WSR-88D, and GOES-14 Super Rapid Scan Datasets*. *Weather and Forecasting*, *30*(3), 571–590. https://doi.org/10.1175/WAF-D-14-00062.1

Bedka, K., Allen, J. T., Punge, H. J., Kunz, M., & Simanovic, D. (2018). A Long-Term Overshooting Convective Cloud-Top Detection Database over Australia Derived from MTSAT Japanese Advanced Meteorological Imager Observations. *Journal of Applied Meteorology and Climatology*, *57*(4), 937–951. https://doi.org/10.1175/JAMC-D-17-0056.1

Berendes, T. A., Mecikalski, J. R., MacKenzie, W. M., Bedka, K. M., & Nair, U. S. (2008). Convective cloud identification and classification in daytime satellite imagery using standard deviation limited adaptive clustering. *Journal of Geophysical Research: Atmospheres*, *113*(D20), 2008JD010287. https://doi.org/10.1029/2008JD010287

Berman, M. T., Trapp, R. J., Nesbitt, S. W., & Di Girolamo, L. (2024). The Observed Impact of the Lower Stratospheric Thermodynamic Environment on Overshooting Top Characteristics During the RELAMPAGO-CACTI Field Campaign. *Journal of*

Geophysical Research: Atmospheres, *129*(10), e2023JD040348. https://doi.org/10.1029/2023JD040348

Berman, M. T., Trapp, R. J., Nesbitt, S. W., & Di Girolamo, L. (2025). Improved Understanding of How Kinematic and Thermodynamic Environmental Changes Impact Modeled Overshooting Top Characteristics. *Geophysical Research Letters*, *52*(21), e2025GL117993. https://doi.org/10.1029/2025GL117993

Bigelbach, B. C., Mullendore, G. L., & Starzec, M. (2014). Differences in deep convective transport characteristics between quasi-isolated strong convection and mesoscale convective systems using seasonal WRF simulations. *Journal of Geophysical Research: Atmospheres*, *119*(19). https://doi.org/10.1002/2014JD021875

Bissell, D. P., Murillo, E. M., & Mullendore, G. L. (2024). Comparing Distributions of Overshooting Convection in HRRR Forecasts to Observations. *Journal of Geophysical Research: Atmospheres*, *129*(15), e2023JD039973. https://doi.org/10.1029/2023JD039973

Bluestein, H. B., Lindsey, D. T., Bikos, D., Reif, D. W., & Wienhoff, Z. B. (2019). The Relationship between Overshooting Tops in a Tornadic Supercell and Its Radar-Observed Evolution. *Monthly Weather Review*, *147*(11), 4151–4176. https://doi.org/10.1175/mwr-d-19-0159.1

Borque, P., Vidal, L., Rugna, M., Lang, T. J., Nicora, M. G., & Nesbitt, S. W. (2020). Distinctive Signals in 1-min Observations of Overshooting Tops and Lightning Activity in a Severe Supercell Thunderstorm. *Journal of Geophysical Research: Atmospheres*, *125*(20), e2020JD032856. https://doi.org/10.1029/2020JD032856

Brunner, J. C., Ackerman, S. A., Bachmeier, A. S., & Rabin, R. M. (2007). A Quantitative Analysis of the Enhanced-V Feature in Relation to Severe Weather. *Weather and Forecasting*, *22*(4), 853–872. https://doi.org/10.1175/WAF1022.1

Christo, G., Trapp, R., Nesbitt, S., Girolamo, L. D., Wolff, E. C., Homeyer, C. R., & Hong, Y. (2025). The Spatial Area and Other Attributes of GOES-16 Overshooting Tops as Indicators of Potential Hail, *153*, 2121–2137. https://doi.org/10.1175/MWR-D-24-0150.1

Cintineo, J. L., Pavolonis, M. J., Sieglaff, J. M., Wimmers, A., Brunner, J., & Bellon, W. (2020). A Deep-Learning Model for Automated Detection of Intense Midlatitude Convection Using Geostationary Satellite Images. *Weather and Forecasting*, *35*(6), 2567–2588. https://doi.org/10.1175/WAF-D-20-0028.1

Community, tobac, Brunner, K., Freeman, S. W., Jones, W. K., Kukulies, J., Senf, F., et al. (2025, December 22). tobac - Tracking and Object-based Analysis of Clouds. Zenodo. https://doi.org/10.5281/zenodo.18012838

Cooney, J. W., Bowman, K. P., Homeyer, C. R., & Fenske, T. M. (2018). Ten Year Analysis of Tropopause-Overshooting Convection Using GridRad Data. *Journal of Geophysical Research: Atmospheres*, *123*(1), 329–343. https://doi.org/10.1002/2017JD027718

Cooney, J. W., Bedka, K. M., Liles, C. A., & Homeyer, C. R. (2025). Automated Detection of Overshooting Tops and Above-Anvil Cirrus Plumes within Geostationary Imagery Using Deep Learning. *Artificial Intelligence for the Earth Systems*, *4*(2), e240037. https://doi.org/10.1175/AIES-D-24-0037.1

Dauhut, T., & Hohenegger, C. (2022). The Contribution of Convection to the Stratospheric Water Vapor: The First Budget Using a Global Storm-Resolving Model. *Journal of*

Geophysical Research: Atmospheres, *127*(5), e2021JD036295. https://doi.org/10.1029/2021JD036295

Dessler, A. E., & Sherwood, S. C. (2004). Effect of convection on the summertime extratropical lower stratosphere: Extratropical Convection and the Lower Stratosphere. *Journal of Geophysical Research: Atmospheres*, *109*(D23). https://doi.org/10.1029/2004JD005209

Dolan, B., Kollias, P., Van Den Heever, S. C., Rasmussen, K. L., Oue, M., Luke, E., et al. (2023). Time Resolved Reflectivity Measurements of Convective Clouds. *Geophysical Research Letters*, *50*(22), e2023GL105723. https://doi.org/10.1029/2023GL105723

Dworak, R., Bedka, K., Brunner, J., & Feltz, W. (2012). Comparison between GOES-12 Overshooting-Top Detections, WSR-88D Radar Reflectivity, and Severe Storm Reports. *Weather and Forecasting*, *27*(3), 684–699. https://doi.org/10.1175/waf-d-11-00070.1

Freeman, S. W., Brunner, K., Jones, W. K., Kukulies, J., Senf, F., Stier, P., & Van Den Heever, S. C. (2024). Advancing Our Understanding of Cloud Processes and Their Role in the Earth System through Cloud Object Tracking. *Bulletin of the American Meteorological Society*, *105*(1), E297–E299. https://doi.org/10.1175/BAMS-D-23-0204.1

Fujita, T. T. (1974). Overshooting Thunderheads Observed From ATS and LEARJET.

Gordon, A. E., & Homeyer, C. R. (2022). Sensitivities of Cross-Tropopause Transport in Midlatitude Overshooting Convection to the Lower Stratosphere Environment. *Journal of Geophysical Research: Atmospheres*, *127*(13), e2022JD036713. https://doi.org/10.1029/2022JD036713

Gordon, A. E., Homeyer, C. R., Smith, J. B., Ueyama, R., Dean-Day, J. M., Atlas, E. L., et al. (2024). Airborne observations of upper troposphere and lower stratosphere composition

change in active convection producing above-anvil cirrus plumes. *Atmospheric Chemistry and Physics*, *24*(13), 7591–7608. https://doi.org/10.5194/acp-24-7591-2024

Griffin, S. M., Bedka, K. M., & Velden, C. S. (2016). A Method for Calculating the Height of Overshooting Convective Cloud Tops Using Satellite-Based IR Imager and CloudSat Cloud Profiling Radar Observations. *Journal of Applied Meteorology and Climatology*, *55*(2), 479–491. https://doi.org/10.1175/JAMC-D-15-0170.1

Hartung, D. C., Sieglaff, J. M., Cronce, L. M., & Feltz, W. F. (2013). An Intercomparison of UW Cloud-Top Cooling Rates with WSR-88D Radar Data. *Weather and Forecasting*, *28*(2), 463–480. https://doi.org/10.1175/WAF-D-12-00021.1

van den Heever, S. C. (2021, November 5). NASA selects new mission to study storms, impacts on climate models. NASA Earth. Retrieved from https://www.nasa. gov/press-release/nasa-selects-new-mission-to-study-storms-impacts-on-climate-models

Heikenfeld, M., Marinescu, P. J., Christensen, M., Watson-Parris, D., Senf, F., Van Den Heever, S. C., & Stier, P. (2019). tobac 1.2: towards a flexible framework for tracking and analysis of clouds in diverse datasets. *Geoscientific Model Development*, *12*(11), 4551–4570. https://doi.org/10.5194/gmd-12-4551-2019

Holton, J. R., Haynes, P. H., McIntyre, M. E., Douglass, A. R., Rood, R. B., & Pfister, L. (1995). Stratosphere-troposphere exchange. *Reviews of Geophysics*, *33*(4), 403–439. https://doi.org/10.1029/95RG02097

Homeyer, C. R., Pan, L. L., Dorsi, S. W., Avallone, L. M., Weinheimer, A. J., O'Brien, A. S., et al. (2014). Convective transport of water vapor into the lower stratosphere observed during double-tropopause events. *Journal of Geophysical Research: Atmospheres*, *119*(18), 10,941-10,958. https://doi.org/10.1002/2014JD021485

Homeyer, C. R., McAuliffe, J. D., & Bedka, K. M. (2017). On the Development of Above-Anvil Cirrus Plumes in Extratropical Convection. *Journal of the Atmospheric Sciences*, *74*(5), 1617–1633. https://doi.org/10.1175/JAS-D-16-0269.1

Homeyer, C. R., Smith, J. B., Bedka, K. M., Bowman, K. P., Wilmouth, D. M., Ueyama, R., et al. (2023). Extreme Altitudes of Stratospheric Hydration by Midlatitude Convection Observed During the DCOTSS Field Campaign. *Geophysical Research Letters*, *50*(18), e2023GL104914. https://doi.org/10.1029/2023GL104914

Illingworth, A. J., Barker, H. W., Beljaars, A., Ceccaldi, M., Chepfer, H., Clerbaux, N., et al. (2015). The EarthCARE Satellite: The Next Step Forward in Global Measurements of Clouds, Aerosols, Precipitation, and Radiation. *Bulletin of the American Meteorological Society*, *96*(8), 1311–1332. https://doi.org/10.1175/BAMS-D-12-00227.1

Itterly, K. F., Bedka, K. M., Homeyer, C. R., & Khlopenkov, K. (2025). Quantifying Tropopause-Overshooting Volume From Satellite and Radar Observations During the DCOTSS 2021 and 2022 Campaigns. *Journal of Geophysical Research: Atmospheres*, *130*(7), e2024JD042418. https://doi.org/10.1029/2024JD042418

Jellis, D., Bowman, K. P., & Rapp, A. D. (2023). Lifetimes of Overshooting Convective Events Using High-Frequency Gridded Radar Composites. *Monthly Weather Review*, *151*(8), 1979–1992. https://doi.org/10.1175/MWR-D-23-0032.1

Jensen, E. J., Pan, L. L., Honomichl, S., Diskin, G. S., Krämer, M., Spelten, N., et al. (2020). Assessment of Observational Evidence for Direct Convective Hydration of the Lower Stratosphere. *Journal of Geophysical Research: Atmospheres*, *125*(15), e2020JD032793. https://doi.org/10.1029/2020JD032793

Khlopenkov, K. V., Bedka, K. M., Cooney, J. W., & Itterly, K. (2021). Recent Advances in Detection of Overshooting Cloud Tops From Longwave Infrared Satellite Imagery. *Journal of Geophysical Research: Atmospheres*, *126*(14), e2020JD034359. https://doi.org/10.1029/2020JD034359

Kim, M., Lee, J., & Im, J. (2018). Deep learning-based monitoring of overshooting cloud tops from geostationary satellite data. *GIScience & Remote Sensing*, *55*(5), 763–792. https://doi.org/10.1080/15481603.2018.1457201

Liu, C., & Zipser, E. J. (2005). Global distribution of convection penetrating the tropical tropopause. *Journal of Geophysical Research: Atmospheres*, *110*(D23), 2005JD006063. https://doi.org/10.1029/2005JD006063

Liu, N., Liu, C., & Hayden, L. (2020). Climatology and Detection of Overshooting Convection From 4 Years of GPM Precipitation Radar and Passive Microwave Observations. *Journal of Geophysical Research: Atmospheres*, *125*(7), e2019JD032003. https://doi.org/10.1029/2019JD032003

Manney, G. L., Hegglin, M. I., Lawrence, Z. D., Wargan, K., Millán, L. F., Schwartz, M. J., et al. (2017). Reanalysis comparisons of upper tropospheric–lower stratospheric jets and multiple tropopauses. *Atmospheric Chemistry and Physics*, *17*(18), 11541–11566. https://doi.org/10.5194/acp-17-11541-2017

Marion, G. R., Trapp, R. J., & Nesbitt, S. W. (2019). Using Overshooting Top Area to Discriminate Potential for Large, Intense Tornadoes. *Geophysical Research Letters*, *46*(21), 12520–12526. https://doi.org/10.1029/2019GL084099

Mecikalski, J. R., Sandmæl, T. N., Murillo, E. M., Homeyer, C. R., Bedka, K. M., Apke, J. M., & Jewett, C. P. (2021). Random Forest Model to Assess Predictor Importance and

Nowcast Severe Storms using High-Resolution Radar–GOES Satellite–Lightning Observations. *Monthly Weather Review*. https://doi.org/10.1175/MWR-D-19-0274.1

Mikuš, P., & Strelec Mahović, N. (2013). Satellite-based overshooting top detection methods and an analysis of correlated weather conditions. *Atmospheric Research*, *123*, 268–280. https://doi.org/10.1016/j.atmosres.2012.09.001

O'Neill, M. E., Orf, L., Heymsfield, G. M., & Halbert, K. (2021). Hydraulic jump dynamics above supercell thunderstorms. *Science*, *373*(6560), 1248–1251. https://doi.org/10.1126/science.abh3857

Pan, L. L., Homeyer, C. R., Honomichl, S., Ridley, B. A., Weisman, M., Barth, M. C., et al. (2014). Thunderstorms enhance tropospheric ozone by wrapping and shedding stratospheric air: Thunderstorms Enhance Tropospheric Ozone. *Geophysical Research Letters*, *41*(22), 7785–7790. https://doi.org/10.1002/2014GL061921

Phoenix, D. B., Homeyer, C. R., Barth, M. C., & Trier, S. B. (2020). Mechanisms Responsible for Stratosphere-to-Troposphere Transport Around a Mesoscale Convective System Anvil. *Journal of Geophysical Research: Atmospheres*, *125*(10). https://doi.org/10.1029/2019JD032016

Poulida, O., Dickerson, R. R., & Heymsfield, A. (1996). Stratosphere-troposphere exchange in a midlatitude mesoscale convective complex: 1. Observations. *Journal of Geophysical Research: Atmospheres*, *101*(D3), 6823–6836. https://doi.org/10.1029/95JD03523

Prasanth, S., Haddad, Z. S., Sawaya, R. C., Sy, O. O., Van Den Heever, M., Narayana Rao, T., & Hristova-Veleva, S. (2023). Quantifying the Vertical Transport in Convective Storms Using Time Sequences of Radar Reflectivity Observations. *Journal of Geophysical*

Research: Atmospheres, *128*(10), e2022JD037701. https://doi.org/10.1029/2022JD037701

Proud, Simon R. (2015). Analysis of overshooting top detections by Meteosat Second Generation: a 5-year dataset. *Quarterly Journal of the Royal Meteorological Society*, *141*(688), 909–915. https://doi.org/10.1002/qj.2410

Proud, Simon Richard, & Bachmeier, S. (2021). Record-Low Cloud Temperatures Associated With a Tropical Deep Convective Event. *Geophysical Research Letters*, *48*(6), e2020GL092261. https://doi.org/10.1029/2020GL092261

Punge, H. J., Bedka, K. M., Kunz, M., & Reinbold, A. (2017). Hail frequency estimation across Europe based on a combination of overshooting top detections and the ERA-INTERIM reanalysis. *Atmospheric Research*, *198*, 34–43. https://doi.org/10.1016/j.atmosres.2017.07.025

Ritman, M., Jones, W., & Stier, P. (2026, February 4). Convective controls on anvil cloud evolution in the ICON km-scale global climate model. Clouds and Precipitation/Atmospheric Modelling and Data Analysis/Troposphere/Physics (physical properties and processes). https://doi.org/10.5194/egusphere-2026-580

Sandmæl, T. N., Homeyer, C. R., Bedka, K. M., Apke, J. M., Mecikalski, J. R., & Khlopenkov, K. (2019). Evaluating the Ability of Remote Sensing Observations to Identify Significantly Severe and Potentially Tornadic Storms. *Journal of Applied Meteorology and Climatology*, *58*(12), 2569–2590. https://doi.org/10.1175/JAMC-D-18-0241.1

Scarino, B., Itterly, K., Bedka, K., Homeyer, C. R., Allen, J., Bang, S., & Cecil, D. (2023). Deriving Severe Hail Likelihood from Satellite Observations and Model Reanalysis

Parameters Using a Deep Neural Network. *Artificial Intelligence for the Earth Systems*, *2*(4), 220042. https://doi.org/10.1175/AIES-D-22-0042.1

Senf, F., Dietzsch, F., Hünerbein, A., & Deneke, H. (2015). Characterization of Initiation and Growth of Selected Severe Convective Storms over Central Europe with MSG-SEVIRI. *Journal of Applied Meteorology and Climatology*, *54*(1), 207–224. https://doi.org/10.1175/JAMC-D-14-0144.1

Setvák, M., Bedka, K., Lindsey, D. T., Sokol, A., Charvát, Z., Šťástka, J., & Wang, P. K. (2013a). A-Train observations of deep convective storm tops. *Atmospheric Research*, *123*, 229–248. https://doi.org/10.1016/j.atmosres.2012.06.020

Setvák, M., Bedka, K., Lindsey, D. T., Sokol, A., Charvát, Z., Šťástka, J., & Wang, P. K. (2013b). A-Train observations of deep convective storm tops. *Atmospheric Research*, *123*, 229–248. https://doi.org/10.1016/j.atmosres.2012.06.020

Sokolowsky, G. A., Freeman, S. W., Jones, W. K., Kukulies, J., Senf, F., Marinescu, P. J., et al. (2024). *tobac* v1.5: introducing fast 3D tracking, splits and mergers, and other enhancements for identifying and analysing meteorological phenomena. *Geoscientific Model Development*, *17*(13), 5309–5330. https://doi.org/10.5194/gmd-17-5309-2024

Solomon, S., Rosenlof, K. H., Portmann, R. W., Daniel, J. S., Davis, S. M., Sanford, T. J., & Plattner, G.-K. (2010). Contributions of Stratospheric Water Vapor to Decadal Changes in the Rate of Global Warming. *Science*, *327*(5970), 1219–1223. https://doi.org/10.1126/science.1182488

Takahashi, H., & Luo, Z. J. (2014). Characterizing tropical overshooting deep convection from joint analysis of CloudSat and geostationary satellite observations. *Journal of*

Geophysical Research: Atmospheres, *119*(1), 112–121. https://doi.org/10.1002/2013JD020972

Thiery, W., Davin, E. L., Seneviratne, S. I., Bedka, K., Lhermitte, S., & Van Lipzig, N. P. M. (2016). Hazardous thunderstorm intensification over Lake Victoria. *Nature Communications*, *7*(1), 12786. https://doi.org/10.1038/ncomms12786

Tinney, E. N., & Homeyer, C. R. (2021). A 13-year Trajectory-Based Analysis of Convection-Driven Changes in Upper Troposphere Lower Stratosphere Composition Over the United States. *Journal of Geophysical Research: Atmospheres*, *126*(3), e2020JD033657. https://doi.org/10.1029/2020JD033657

Trapp, R. J., Marion, G. R., & Nesbitt, S. W. (2017a). The Regulation of Tornado Intensity by Updraft Width. *Journal of the Atmospheric Sciences*, *74*(12), 4199–4211. https://doi.org/10.1175/JAS-D-16-0331.1

Trapp, R. J., Marion, G. R., & Nesbitt, S. W. (2017b). The Regulation of Tornado Intensity by Updraft Width. *Journal of the Atmospheric Sciences*, *74*(12), 4199–4211. https://doi.org/10.1175/JAS-D-16-0331.1

Ueyama, R., Schoeberl, M., Jensen, E., Pfister, L., Park, M., & Ryoo, J.-M. (2023). Convective Impact on the Global Lower Stratospheric Water Vapor Budget. *Journal of Geophysical Research: Atmospheres*, *128*(6), e2022JD037135. https://doi.org/10.1029/2022JD037135